Microstructure and Crystallization Behavior in Bulk Glass Forming Alloys

Thesis by

Sven Bossuyt

In partial fulfillment of the requirements for the degree of

Doctor of Philosophy

California Institute of Technology

Pasadena, California

2001

(submitted November 3 2000)

Acknowledgements

Caltech is a remarkable place. I wish to thank everybody who helped make the five years I spent as a graduate student here both fruitful and enjoyable.

First and foremost, my gratitude goes to Professor Bill Johnson for giving me the opportunity to pursue my doctorate at Caltech. It has been a pleasure working with him. Due to his exceptional intuition and quickness of thought, discussing results and ideas with him always results in refreshing insights.

I also benefited from stimulating discussions, collaboration on experiments, demonstrations of equipment, and general companionship provided by Channing Ahn, Uta Bete, Peter Bogdanov, Jonathan Burrows, Claudine Chen, Dale Conner, Rich Dandliker, Prof. Pierre Desré, Carol Garland, Stephen Glade, Charles Hays, Adrian Hightower, Jörg Löffler, Mike Manley, Jan Schroers, Valerie Scruggs, Ben Shapiro, Laura Sinclair, Andy Waniuk, and Chuk Witham, among others.

Financial support was provided by the Belgian American Educational Foundation and the U.S. Department of Energy (Grant No. DEFG0386ER45242).

Last, but not least, I must acknowledge the support of my family. My parents have always encouraged their children to be curious and creative, and to believe in themselves. My wife helps me to do this, and makes me happy.

Abstract

The solidification microstructure in wedge-shaped castings of Cu-Ni-Ti-Zr glass forming alloys is investigated, while the composition was systematically varied. Near the critical thickness for glass formation, a spatially inhomogeneous dispersion of nanocrystals is observed, where spherical regions contain a much higher density of nanocrystals than the surrounding material. This microstructure is inconsistent with the prevalent theories for crystallization in metallic glasses, which predict a spatially uniform distribution of crystals.

The spatial localization of the nucleation density is attributed to a recalescence instability. Linear stability analysis of the equations for heat flow coupled with crystal nucleation and growth reveals that at low temperature recalescence can occur locally, triggered by a small fluctuation in the early stages of the crystallization process, because in deeply undercooled liquids the nucleation rate increases with temperature. The localized recalescence events and their interaction accelerate crystallization; consequently they are important in determining the glass forming ability as well as the microstructure of these alloys.

The composition dependence of the critical thickness for glass formation, determined from the observed microstructures, and in situ small angle scattering results indicate that the crystallization occurs in several steps, involving competing crystalline phases.

Contents

1. Introduction

2. Experimental Techniques

3. Microstructure

4. Crystallization Kinetics

5. Alloy Development

6. Annealing

7. Summary

A. Appendices

References

Figures

1. Introduction

Definition of glass

In general, when a liquid is cooled, its free volume decreases, and the amount of short range order increases. As a result the mobility in the liquid decreases, e.g., diffusion constants decrease and the viscosity increases [1]. The time scale for changing the configuration of the liquid becomes longer. When this time scale exceeds the time scale of the experiment, the material behaves more like a solid than like a liquid. This transition, where the time scale for sampling the configuration space of the liquid crosses over the time scale of the experiment, is called the glass transition.

A glass is then defined as a liquid cooled below its glass transition temperature. The glass transition behaves like a second order phase transition, but it is not strictly a phase transition in the thermodynamic sense. The difference between the glass and the liquid is an issue of kinetics rather than thermodynamics. In the framework of statistical mechanics, the configuration spaces of the glass and the liquid are fundamentally the same. The configuration space of the glass appears smaller because ergodicity breaks down on the time scale of the experiment. A glass is therefore, by its definition, not an equilibrium phase.

For most metals and alloys, the equilibrium state at room temperature is a crystalline phase or a mixture of crystalline phases [2]. At high temperatures the liquid is thermodynamically stable. Below the liquidus temperature there is a thermodynamic driving force for crystallization, so the liquid is metastable. Whether or not crystals form depends on the crystallization kinetics. Below the glass transition temperature the liquid is still metastable, but the crystallization kinetics are so sluggish that it would take essentially forever to form a crystal. The requirement for forming a glass is therefore to be able to avoid crystallization while cooling the liquid from above the liquidus temperature to below the glass transition.

Glass formation

Since the crystalline phase introduces order which was absent in the liquid phase, there can not be a catastrophic crystallization instability like there is for melting. Crystallization must occur via a process of nucleation and growth. It is not necessary to completely eliminate nucleation in order to make a glass; if the crystallized volume fraction is below the detection limit inherent in the experiment, the material is amorphous for all practical purposes. The cooling rate necessary to achieve this depends on the nucleation and growth rates and their temperature dependence.

In the absence of convection or some adiabatic cooling mechanism, the cooling rate is limited by thermal conduction in the liquid, which scales with the square of the smallest sample dimension [3]. As a result, a critical cooling rate for glass formation corresponds to a critical thickness for glass formation. This critical thickness for glass formation can be used to quantify the concept of glass forming ability. It is directly related to the critical cooling rate for glass formation, but easier to determine experimentally —except for very good glass formers, where the critical thickness is large and the critical cooling rate not very difficult to achieve.

Glass forming materials

The most familiar glass forming materials are ceramics, network silicates to be exact. Crystallization kinetics in network silicates are so sluggish that glass can be formed even at geological cooling rates [4]. The manufacture of household objects from silicate glass dates back at least to 2500 B.C., although the transparent variety is a much more recent development [5]. Network silicates are ideal glass forming materials, because the rearrangement of the silicate chains into a crystalline network is a very slow process.

Polymer melts also consist of a tangle of chains that is difficult to rearrange into a crystal. In some polymers with an aperiodic molecular structure or where the chains form a covalently bonded network it is not possible to form a crystal at all. Even crystalline polymers usually have a highly non-equilibrium microstructure with a significant volume fraction of an amorphous phase between crystals [6].

Many other ceramic and organic glasses have been found, but metallic glasses remain somewhat of a novelty. Metallic glass was first produced from the melt in 1960 at Caltech [7] by splat quenching Au-Si alloys near the eutectic composition.

Many other alloys have been vitrified since then using rapid quenching techniques [8-10]. The soft magnetic properties of Fe-B based glass ribbons produced by planar flow casting have led to their use in a wide range of industrial applications [11]. But the need for high cooling rates has nevertheless placed constraints on scientific experiments and practical applications. The recent discovery of bulk metallic glasses, such as $La_{55}Al_{25}Ni_{20}$ [12], $Zr_{65}Al_{7.5}Ni_{10}Cu_{17.5}$ [13], $Zr_{41.2}Ti_{13.8}Cu_{12.5}Ni_{10}Be_{22.5}$ [14], $Pd_{40}Cu_{30}Ni_{10}P_{20}$ [15], $Zr_{58.5}Nb_{2.8}Cu_{15.6}Ni_{12.8}Al_{10.3}$ [16] and related alloys has enabled practical applications as well as studies of previously inaccessible properties of undercooled liquids.

The initial objective for this work was alloy development: finding the composition with the best glass forming ability in a given alloy system. A systematic study of glass forming ability as a function of alloy composition would be undertaken with the dual aim of improving our understanding of the requirements for making bulk metallic glasses and testing techniques for locating the optimum composition in newly discovered families of glass forming alloys. The Cu-Ni-Ti-Zr system was chosen for this work, because $Cu_{47}Ni_8Ti_{34}Zr_{11}$ (Vit101) [17] is known to be a relatively good glass forming composition, and the system contains “only” 4 components[*].

---

[*] The complexity of the optimization problem increases exponentially with the dimensionality of the composition space, so systems with fewer components are more amenable to a systematic alloy development process. This is discussed in detail under “Empirical optimization” on page 59 and “Geometry of composition spaces” on page 80.

The intention was to identify a critical casting thickness for glass formation, measure how it changes with small changes in composition, extrapolate these results to find a better glass forming composition, and repeat this process until a local optimum was found. However, the microstructure at the critical casting thickness and its composition dependence proved to be much more complex than expected on the basis of prevalent theories concerning crystallization behavior in glass forming alloys.

Microstructure and crystallization behavior

Paradoxically, this work about a non-crystalline form of matter deals almost exclusively with crystallization. Glass formation can only occur if crystals do not form. The glass forming ability of an alloy is therefore related more to the properties of the crystalline phases that do not form, than to the properties of the glass that forms. It is the crystallization behavior at the critical cooling rate, i.e., in the limit where crystallization does not occur, that must be understood in order to understand glass formation. The microstructure of samples that solidified at cooling rates close to this critical cooling rate holds important clues to the crystallization behavior.

Alloys with different compositions close to Vit101 were studied in this work, by examining the solidification microstructure in samples where the cooling rate varied along the sample. Chapter 2 describes the sample preparation methods and experimental techniques that were used. Chapter 3 gives an overview of the observed microstructures, with particular emphasis on the features of the microstructure close to the critical cooling rate for glass formation. Chapter 4 starts with a presentation of the classical theory for crystal nucleation and growth, pointing out its shortcomings and the discrepancies with the microstructures described in chapter 3. An extension of this theory is then proposed, introducing the concept of localized recalescence to resolve these discrepancies. A discussion, within this framework, of the variations in crystallization behavior with composition leads to chapter 5 about alloy development. Finally, in chapter 6, results of in situ experiments on the crystallization behavior during annealing of amorphous samples are presented and discussed.

2. Experimental Techniques

2.1. Alloying

Starting materials

Ingots of a variety of alloys in the Cu-Ni-Ti-Zr system, with compositions close to the bulk glass forming alloy $Cu_{47}Ni_{8}Ti_{34}Zr_{11}$ (Vit101) [17], were prepared by induction melting the constituent elements under inert atmosphere. In order to keep the oxygen content of the alloys as low as possible, the highest purity Zr and Ti crystal bar available from Wah-Chang Teledyne, with <50 ppm oxygen, were used. Cu and Ni were supplied by CERAC, item Nos. C-1131 and N-2009 respectively.

Induction melting procedure

A typical sequence of events for preparing an alloy by induction melting is described below:

- The alloying elements are weighed out. Small pieces are cut off with wire cutters or added to adjust the amount of each of the elements until the desired alloy composition is obtained.
- Before melting, the alloying elements are cleaned by sonication in acetone and then in ethanol.

- The elements to be alloyed and the titanium getter are arranged* on separate troughs in the copper boat, which is placed inside the fused silica tube, as shown in Fig. 2.1.
- The tube is evacuated to $<1\times10^{-2}$ mbar and backfilled with ultra high purity (UHP, 99.9999%) argon. It is then evacuated to $<1\times10^{-5}$ mbar.
- The Ti getter is heated to approximately 800 °C (glowing red-hot) for 5 min. Then the sample is heated slowly while monitoring the vacuum gauge readout.
- When no more outgassing is observed, the sample is allowed to cool down and the tube is backfilled again with UHP argon.
- The Ti getter is heated red-hot again for 5 min and allowed to cool down. The getter is checked for signs of oxidation and heated red-hot for another 5 min.
- The elements are then heated until they are all molten together.
- The crystallization of the alloy is observed while it cools down. The alloy is molten again and kept molten for 15 min. If the crystallization behavior is different from the first time, the sample is molten again for a longer time and/or at higher power until a consistent crystallization behavior emerges.
- The sample is allowed to cool down, removed from the apparatus and weighed to check for any weight change.

---

* If all elements are alloyed at once, Ni and Zr are the last elements to melt completely. To avoid having to melt the alloy for a long time, the elements were arranged with Ni and Zr on one side, and Cu and Ti on the other side of the same trough in the copper boat. The large exothermic heat of mixing of the Ni and Zr assured that these elements were alloyed completely before the Cu and Ti were added.

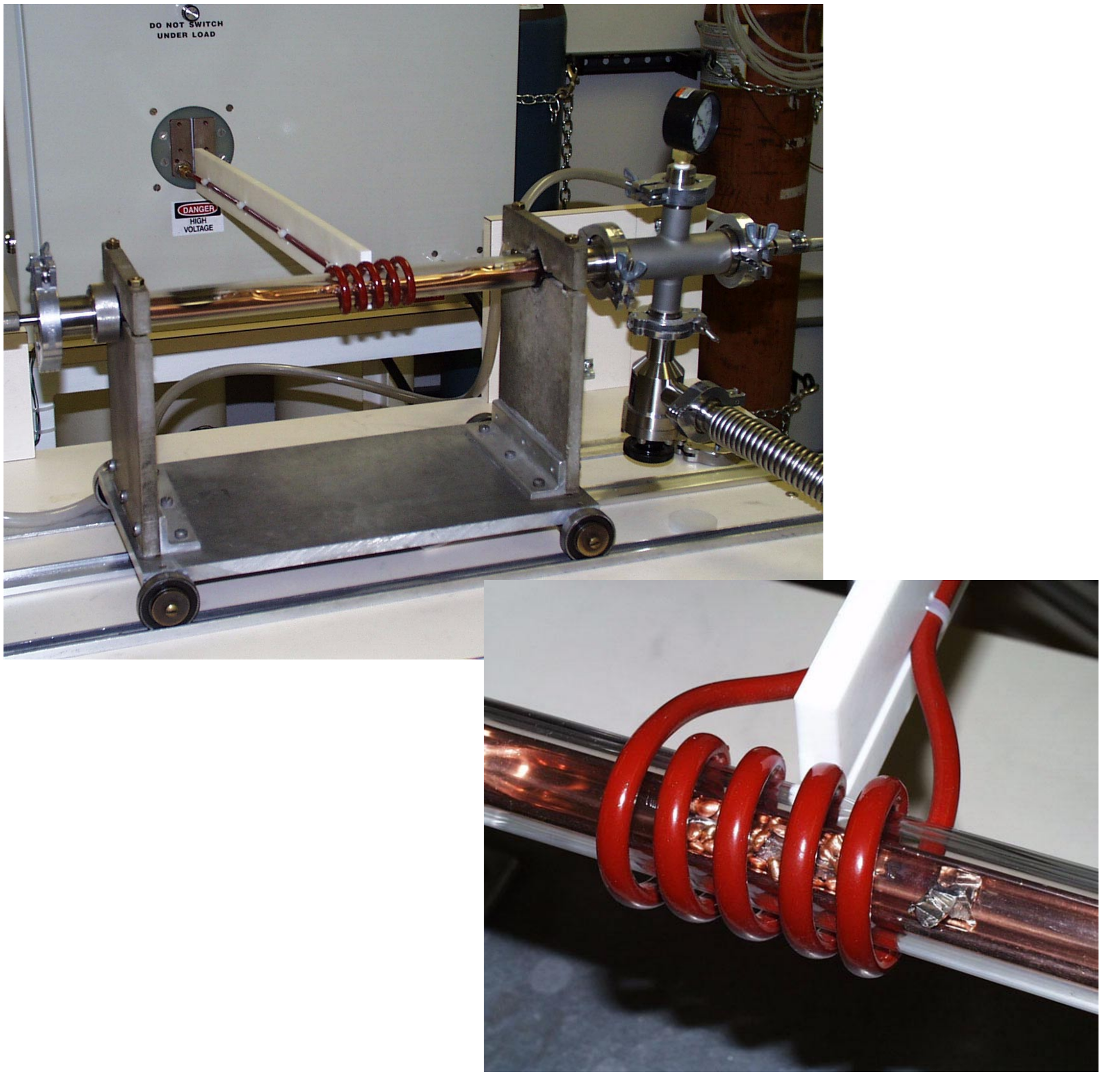

Figure 2.1: induction melting apparatus

> *The sample is molten on a water-cooled copper boat, which is enclosed in a fused silica tube sealed off with vacuum fittings. The induction coil is wrapped around the fused silica tube. Power is provided by a 15 kW Lepel LSS-15 radio frequency generator. A vacuum pumping system is connected to the fittings on the fused silica tube to evacuate the tube and fill it with an inert atmosphere, typically titanium gettered ultra high purity argon. The fused silica tube with the copper boat is supported on a carriage system, so that the boat can be moved freely inside the induction coil.*

Compositions

In order to study the composition dependence of the crystallization behavior in the Vit101 alloy system, a series of alloys were made in which the composition was systematically varied. For each of the alloys, the composition of Vit101 was modified by decreasing the amount of one of the elements by 1 at.% compensated by an increase in the amount of one of the other elements. This results in 12 compositions symmetrically located[*] around Vit101 in composition space, as shown in Fig. 2.2.

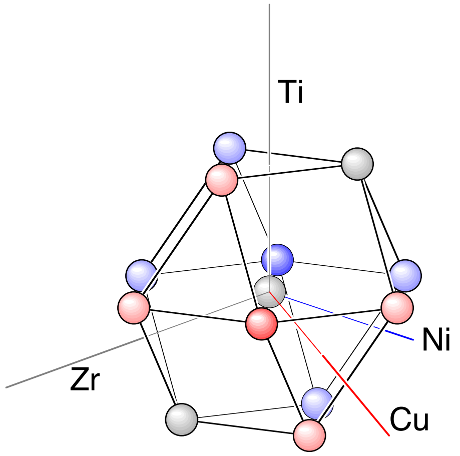

Figure 2.2: alloy compositions

Position in the three-dimensional Cu-Ni-Ti-Zr composition space, relative to Vit101, of the 12 alloys studied in this work. The color code reinforces the depth cues corresponding to the Cu-Ni axis.

---

[*] The compositions are located at the vertices of a cuboctahedron with the Vit101 composition at its center. This is also the geometry of the 12 nearest neighbors of an atom in a face centered cubic lattice.

2.2. Metal mold casting

In order to produce samples solidified under well-defined conditions, pre-alloyed ingots were remelted and injection cast into a copper mold under vacuum. The experimental setup is schematically illustrated in Fig. 2.3.

Injection casting procedure

A typical sequence of events for injection casting an alloy is described below:

- A crucible is made from a length of fused silica tube stock by forming a constriction near one end, leaving an orifice approximately 1 mm in diameter.
- The copper mold is placed inside the vacuum chamber, below the induction heating coil.
- The alloy ingot is inserted in the crucible, which is placed inside the heating coil. The lower end of the crucible fits into an opening in the mold.
- A gas line is fitted to the top of the crucible.
- The vacuum chamber is closed and evacuated to $< 1 \times 10^{-1}$ mbar, flushed repeatedly with UHP Argon, and then evacuated to $< 1 \times 10^{-3}$ mbar.
- The sample is heated slowly to approximately 700 °C (glowing dull red).
- The vacuum valve is closed and the R. F. power to the coil is increased.
- When the alloy is completely molten, the valve on the gas line is opened, ejecting the molten alloy through the orifice in the crucible into the copper mold.
- The sample is allowed to cool down, then the mold is removed from the apparatus, and the sample is removed from the mold.

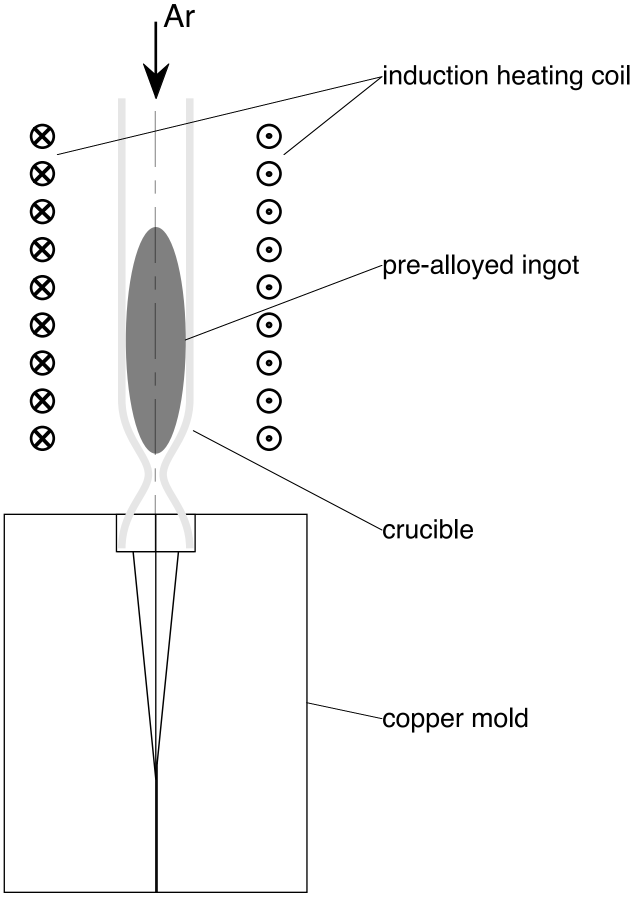

Figure 2.3: injection casting setup

The alloy is contained in a fused silica crucible, open at the top and with a small orifice at the bottom. The pre-alloyed ingot is remelted by induction heating, then ejected from the crucible into the mold by applying gas pressure to the top of the crucible. The metal mold is of a split-mold design machined from OFHC copper. Cooling the mold is not necessary because it has a much larger thermal mass than the sample. The whole assembly resides in a vacuum chamber.

Cooling rates in metal mold casting

The cooling rate obtained by metal mold casting depends primarily on the geometry of the mold. Neglecting convection, i.e., assuming that a quiescent melt of uniform temperature fills the mold instantly, the evolution of the temperature profile in the mold is described by the Fourier heat flow equation:

$$\frac{\partial T}{\partial t} = \frac{1}{\rho c_P} \nabla \bullet (\kappa \nabla T) = \alpha \nabla^2 T , \tag{2.1}$$

where T is temperature, t is time, ρc_P is the heat capacity per unit volume, κ is the thermal conductivity and $\alpha = \kappa / \rho c_P$ is the thermal diffusivity. The boundary conditions can be idealized[*] as a fixed temperature at the mold surface.

A formal solution to the Fourier equation is obtained by using the spectral representation of the Laplacian[†] with these boundary conditions. The coefficient of each of the terms in the spectral representation decays exponentially with a time constant $\tau = 1/(\alpha k^2)$ where $-k^2$ is the eigenvalue of the Laplacian for that term. The physical interpretation of k is the inverse of a characteristic length scale for the temperature variation.

---

[*] Since the thermal conductivity of the copper mold (400 W/m K) is much larger than that of the melt (4 W/m K), and the mold is much more massive (>2 kg) than the sample (a few grams), this is a reasonable approximation provided that the melt remains in good thermal contact with the mold.

[†] The spectral representation of a linear operator amounts to a projection onto the eigenfunctions of the operator. In one dimension, for example, the eigenfunctions of the Laplacian are sine and cosine functions, so that the spectral representation is the familiar Fourier series (See "Solutions to the Fourier heat flow equation" on page 75 for applications).

For long times the solution is dominated by the term with the longest time constant, i.e., the term involving the eigenfunction for which the characteristic length scale is the size of the sample. It leads to an asymptotic cooling rate $\dot{T} = T/\tau = \alpha T k^2$. This is consistent with the scaling law $\dot{T} \propto \alpha T/L^2$, where L is the characteristic length scale for the problem, which can be deduced from dimensional analysis of the Fourier heat flow equation and, as such, is more generally valid.

Wedge-shaped samples

In order to evaluate the solidification microstructure as a function of cooling rate, a mold was designed for casting wedge-shaped samples. A technical drawing specifying the mold design is shown in Fig. 2.4. In a wedge geometry, the thickness of the sample varies along its length[*], resulting in a systematic variation of the cooling rate. Near the tip of the wedge, the cooling rate profile depends only on the opening angle of the wedge, so that results for wedges of different sizes can be compared if all three dimensions are scaled uniformly.

For each of the compositions studied, one or more wedge-shaped samples were cast. The as-cast samples were sectioned along their center line using a diamond saw. One half of the sample was then polished for optical microscopy and SEM. The other half was sectioned again, perpendicular to the center line into 1 mm slices, for X-ray diffraction and TEM samples. This is illustrated in Fig. 2.5.

---

[*] A conical geometry could have been used as well, but the wedge-shaped mold is easier to machine.

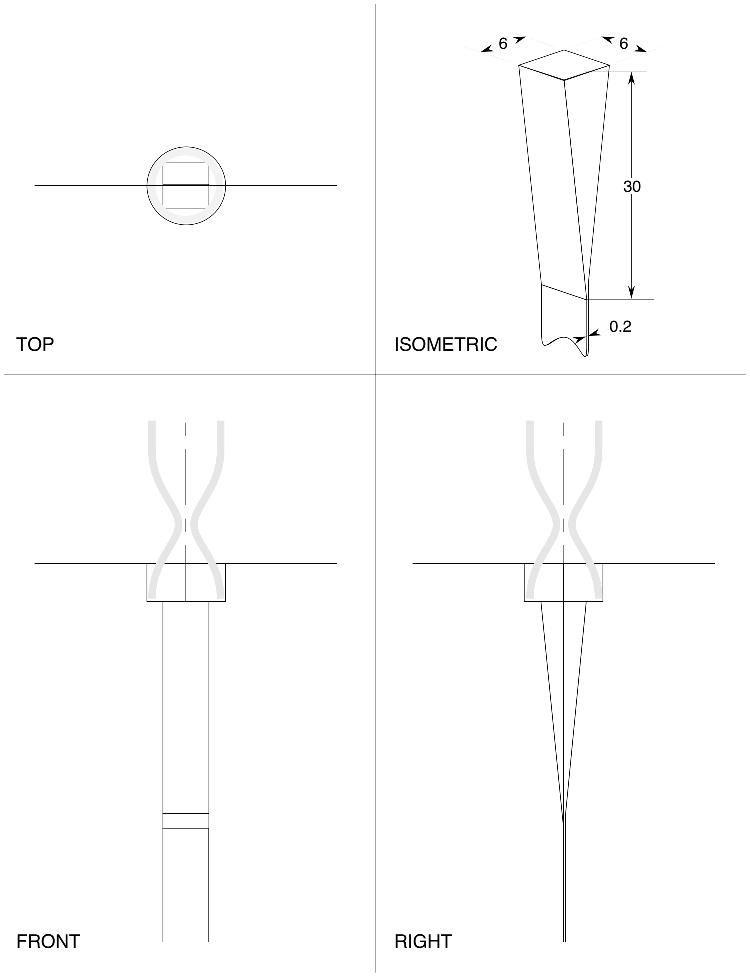

Figure 2.4: drawing of wedge mold

The mold is of a split mold design, machined from OFHC copper bar stock. The resulting wedge-shaped casting is 30 mm long, 6 mm wide, and the thickness varies linearly from 0.2 mm at the tip to 6 mm at the end.

Figure 2.5: overview of wedge-shaped casting usage for sample preparation

Top: wedge-shaped casting, sectioned along center line.

Middle: polished cross section in metallographic mount.

Bottom: slices perpendicular to center line.

Not shown: TEM samples prepared from these slices.

2.3. Microstructure characterization

Metallography

The half of the wedge-shaped casting to be used for metallography was embedded in a polyester mounting compound, Buehler castolite resin No. 20-8120-002 and hardener No. 20-8122-002. In order to fit the sample in the mounting cup the sample was cut in half. Mounting these two halves in the same mount had the added benefit of helping to keep the sample flat during polishing. The resin was cured at 60 °C for 8 to 12 hours. The surface was then ground flat using a succession of SiC grinding papers and polished.

Polishing with diamond paste or alumina slurry resulted in a poor polish with severe pitting of the sample surface. Such pitting can be the result of "pullout," which occurs when polishing with an abrasive of the same size as the microstructure of the material to be polished. With these samples this occurred at all abrasive sizes, presumably because the wide range of cooling rates in the sample results in a wide range of microstructure length scales. Pitting was eliminated by using diamond lapping film instead of a slurry for polishing.

The polished samples were examined on an inverted reflected light microscope using polarized light. Images were acquired in digital form using a TV camera connected to a frame grabber. When the resolution or the field of view of the camera was insufficient, overlapping images were acquired and pasted together using image manipulation software.

Scanning electron microprobe (SEM/microprobe)

Some of the samples used for optical microscopy were subsequently carbon-coated and examined in a JEOL model JXA-733 microprobe equipped with 5 wavelength-dispersive spectrometers. Images were acquired using the backscattered electron detector, with the goal of minimizing any topographical contrast in the image and obtaining an image where contrast is due mainly to variations in composition. Composition measurements were performed with the spectrometers, using the pure metals as standards and the CITZAF correction package [18].

X-ray diffraction

Diffraction patterns were obtained from sections perpendicular to the long axis of the wedge-shaped samples at various thicknesses. The experiments were carried out using Co K-α radiation and an inel CPS-120 curved position sensitive detector. The samples were supported on a glass slide for the measurement. The channel numbers of the output from the inel detector were calibrated as 2θ angles using a polycrystalline silicon diffraction standard.

Transmission electron microscopy (TEM)

A few samples were further investigated by transmission electron microscopy. The microscope used is a Philips model EM430, equipped with a LaB_6 filament.

TEM samples were prepared from the 1 mm slices by ultramicrotomy. Before it is mounted in the microtome, the sample is filed away around the region of interest until only a tip at the region of interest remains. Using the microtome, TEM samples are then sliced from this tip with a diamond knife edge, collecting the samples on the surface of a small water reservoir behind the knife edge. The TEM samples are picked up from the water surface with a holey carbon grid which fits inside the microscope sample holder.

The TEM images shown are dark field electron micrographs obtained with a 70 μm objective aperture selecting intensity from the first diffraction ring. Since the interatomic spacing in the glass is comparable to the interatomic spacing in crystalline phases, any diffraction spots from nanocrystals overlap the diffuse diffraction ring from the amorphous phase. As a result, these dark field conditions highlight crystallites in the corresponding range of orientations, as well as (but more brightly than) the amorphous phase.

2.4. Annealing

Low-temperature crystallization studies were performed by annealing amorphous samples at temperatures slightly above the glass transition. For this purpose, pre-alloyed Vit101 samples were cast into 1 mm thick strips, 10 mm wide and 25 mm long, which were then sectioned into two 10 mm squares using a diamond saw. These squares were wrapped in tantalum foil, sealed in a fused quartz tube under vacuum of $5\times10^{-6}\,\mathrm{mbar}$ or lower, and annealed in a resistively heated tube furnace at various temperatures.

Differential scanning calorimetry (DSC)

A Perkin-Elmer DSC-7 differential scanning calorimeter was used to study the thermal behavior of such pre-annealed Vit101 samples. The DSC scans were taken with a heating rate of 0.333 K/s.

Small angle X-ray scattering (SAXS)

In situ SAXS experiments were performed at the Basic Energy Science Synchrotron Radiation Center (BESSRC) at the Advanced Photon Source (APS), Argonne National Laboratory. SAXS requires X-ray transparent samples, so splat quenched foils, between 30 and 50 μm thick, were prepared. The energy of the photons was 13.5 keV, corresponding approximately to 1 Å wavelength. The raw data from the two-dimensional position sensitive detector was averaged over the azimuthal angle to obtain the radial average scattered intensity which was analyzed.

3. Microstructure

3.1. Metallography

Polished cross sections of wedge-shaped castings of different alloys were observed by optical microscopy. Contrast was obtained by using polarized light. Composite images of typical cross sections are shown in Fig. 3.1 and Fig. 3.2. Similar microstructures are observed for each of the alloy compositions studied. The positions in the sample where these microstructures occur roughly scale with a critical thickness which depends on composition.

Near the tip of the wedge and at the surface, where the cooling rate was highest, the sample is completely amorphous as determined by X-ray diffraction and TEM analysis. Near the base of the wedge, where the cooling rate was lowest, the sample is nearly fully crystallized. In the region between the crystallized part and the fully amorphous part of the sample, spherical features are observed in the optical micrograph, with diameters ranging from $<10\ \mu$m to 300 μm. Similar features have also been observed in other bulk glass forming alloys cooled from the melt, including $Zr_{41.2}Ti_{13.8}Cu_{12.5}Ni_{10}Be_{22.5}$ [19] and $Zr_{58.5}Nb_{2.8}Cu_{15.6}Ni_{12.8}Al_{10.3}$ [20], but they have received little attention. As illustrated in Fig. 3.3, the size and number density of these spheres increase continuously from the amorphous part of the sample, where there are none, to the fully crystallized part, where the spheres coalesce leaving no space in between.

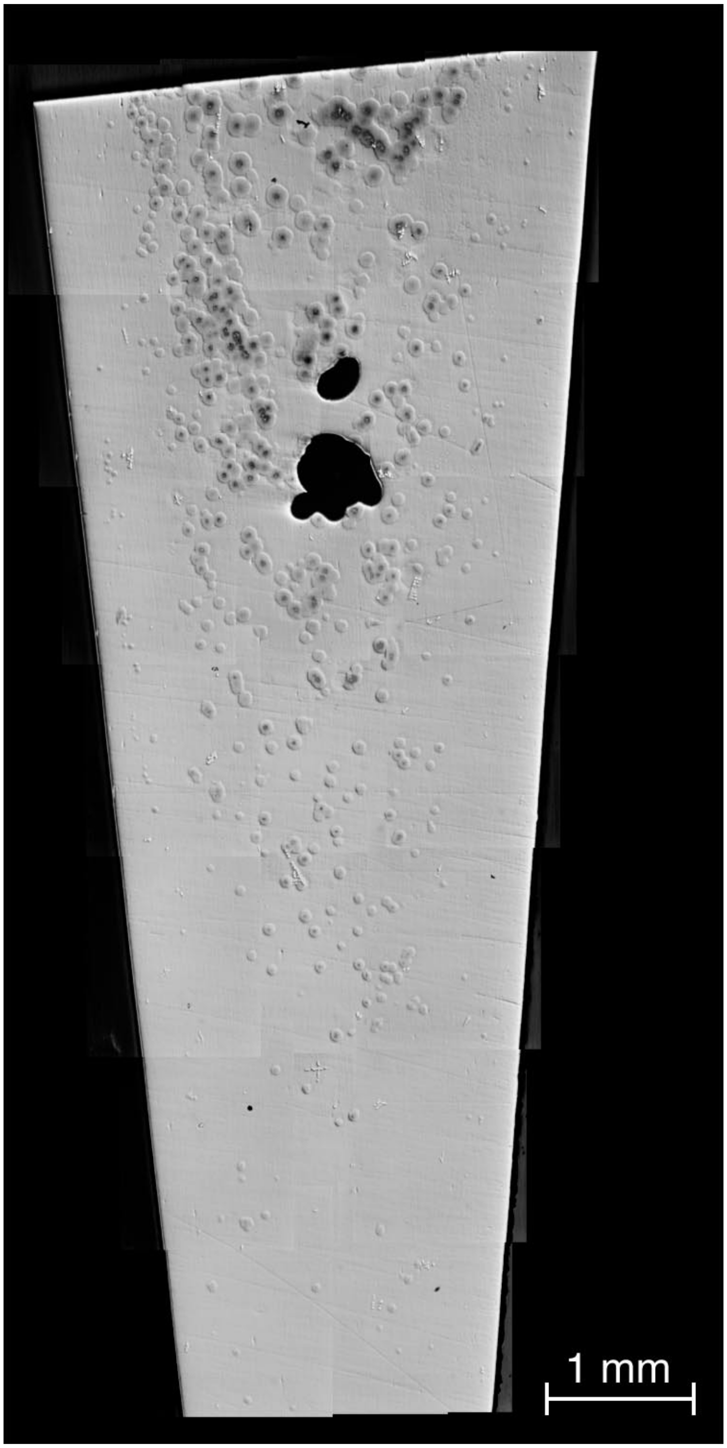

Figure 3.1: optical micrograph of $Cu_{48}Ni_8Ti_{34}Zr_{10}$ *wedge*

Cross section from the center of an as-cast wedge-shaped sample, showing spherical features increasing in size and number density with decreasing cooling rate. The large dark areas in the center are cavities in the sample.

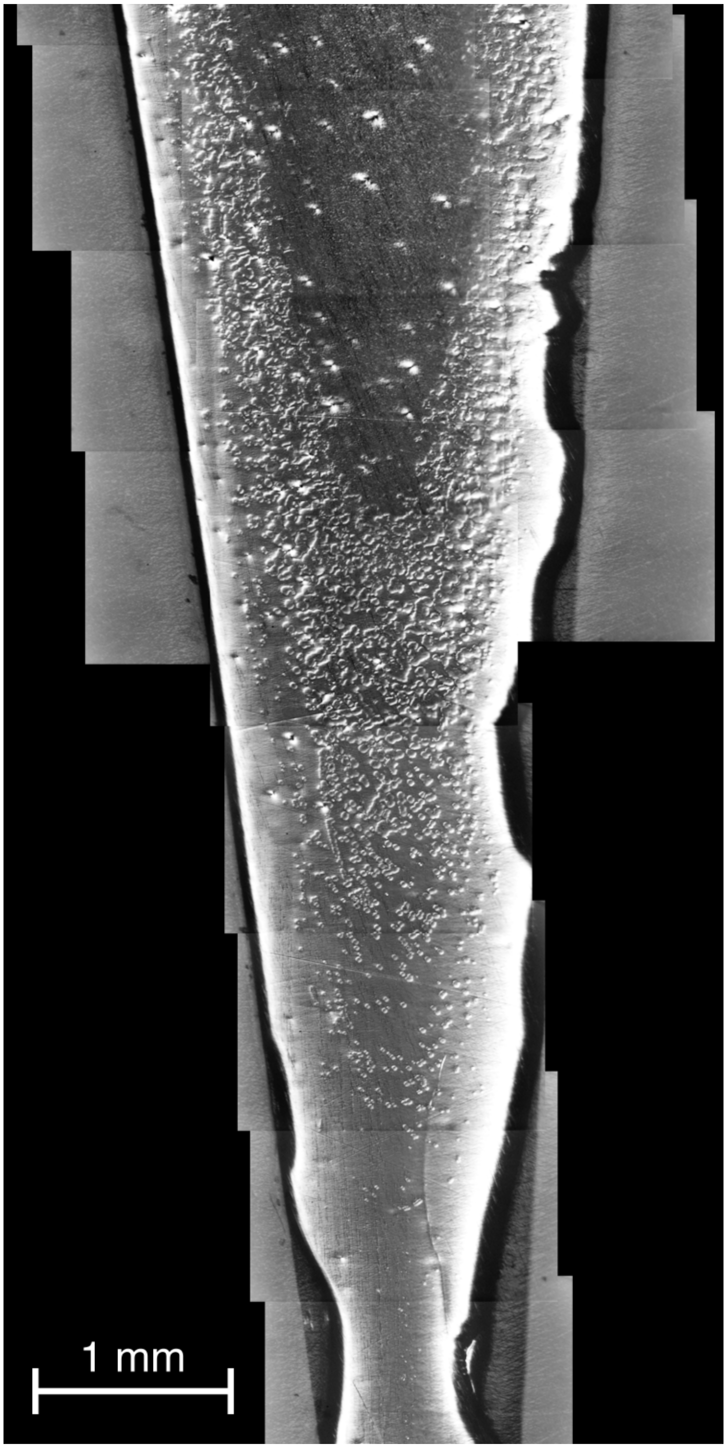

Figure 3.2: optical micrograph of $Cu_{47}Ni_{8}Ti_{34}Zr_{11}$ *(Vit101) wedge*

Cross section from the center of an as-cast wedge-shaped sample, showing spherical features increasing in size and number density with decreasing cooling rate until they coalesce. The edges of this sample were damaged during sectioning.

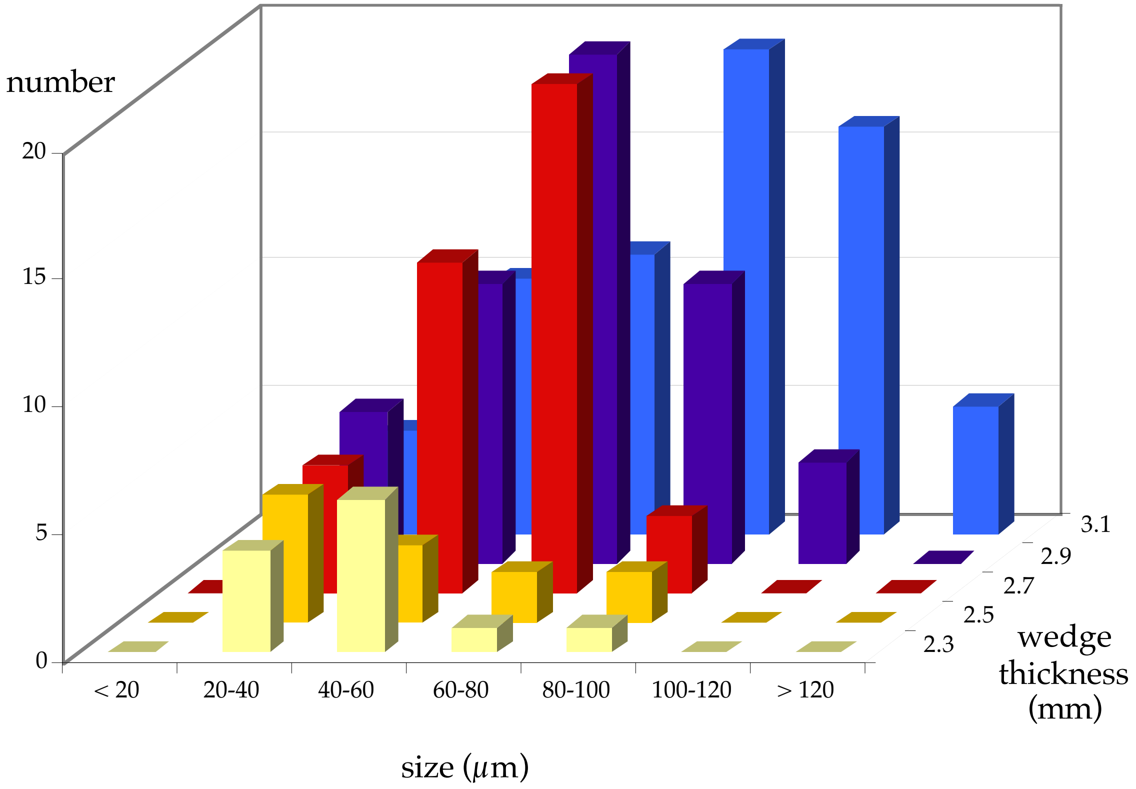

Figure 3.3: size distribution of spherical features[*]

Histogram obtained by dividing the micrograph in Fig. 3.1 into horizontal strips with a height corresponding to 1 mm, and counting the number of circles with diameters in each size range. The indicated thickness is the wedge thickness at the center of each strip. The size and number of the spherical features increase with increasing thickness, i.e., with decreasing cooling rate[†].

[*] *This is actually the size distribution of the circles in the micrograph. It is related to, but not identical with, the size distribution of the spherical features. The conversion gives non-physical results (negative numbers) with this data because the data sets are too small.*

[†] *The cooling rate varies within each of the strips, from very high cooling rates near the edges to a minimum cooling rate in the center. This entire cooling rate profile scales with the inverse square of the wedge thickness.*

In addition to these spherical features, there are also some dendrites visible in Fig. 3.1. The dendrites seem not to have influenced the crystallization of the surrounding material. Dendrites are not observed in some of the other samples with different compositions, while the spherical features were observed in every sample studied. Assuming a definition of glass forming ability that tolerates the presence of a small volume fraction of crystals, it appears that the glass forming ability in the Vit101 alloy system is limited by the formation of the spherical features, and not by the formation of these dendritic crystals.

The thickness where these spherical features occupy a given volume fraction[*] of the sample can then be taken to be a measure of the critical casting thickness for glass formation. The chosen threshold value is of course somewhat arbitrary; using a different threshold value —or a different criterion for glass formation altogether— would result in a slightly different value for the critical casting thickness. This does not hinder comparisons of the critical thickness between different samples, provided that the difference from one criterion to another is similar for each of the samples.

The wedge thickness where the spherical features occupy roughly 5% in the optical micrograph was evaluated for a series of alloys in which the composition was systematically varied. The results are listed in Table 3.1, and represented graphically as a "bubble chart" in Fig. 3.4. No clear trends emerge from this data.

---

[*] If there is no preferred orientation, the fractional area occupied by features in a cross section is equal to their volume fraction.

Table 3.1: variation of critical casting thickness with composition

Composition	critical casting thickness (mm)
$Cu_{47}Ni_8Ti_{34}Zr_{11}$ (Vit101)	1.1
$Cu_{46}Ni_9Ti_{34}Zr_{11}$	2.5
$Cu_{46}Ni_8Ti_{35}Zr_{11}$	4.0
$Cu_{46}Ni_8Ti_{34}Zr_{12}$	3.5
$Cu_{48}Ni_7Ti_{34}Zr_{11}$	2.5
$Cu_{47}Ni_7Ti_{35}Zr_{11}$	1.5
$Cu_{47}Ni_7Ti_{34}Zr_{12}$	3.2
$Cu_{48}Ni_8Ti_{33}Zr_{11}$	1.8
$Cu_{47}Ni_9Ti_{33}Zr_{11}$	3.1
$Cu_{47}Ni_8Ti_{33}Zr_{12}$	3.5
$Cu_{48}Ni_8Ti_{34}Zr_{10}$	2.6
$Cu_{47}Ni_9Ti_{34}Zr_{10}$	5.5
$Cu_{47}Ni_8Ti_{35}Zr_{10}$	3.5

Surprisingly, the central composition (Vit101) is the worst glass former*. One would have expected a local maximum in the critical casting thickness near a good glass forming composition, not a local minimum! There is no immediately obvious direction in composition space which gives a larger improvement in glass

---

* This is not due to experimental error. Several samples with the Vit101 composition were cast successfully, allowing the variability of the critical casting thickness to be estimated at ±20% for successful castings. Unsuccessful castings —e.g., where the crucible broke during casting— resulted in similar or lower critical casting thickness than successful castings.

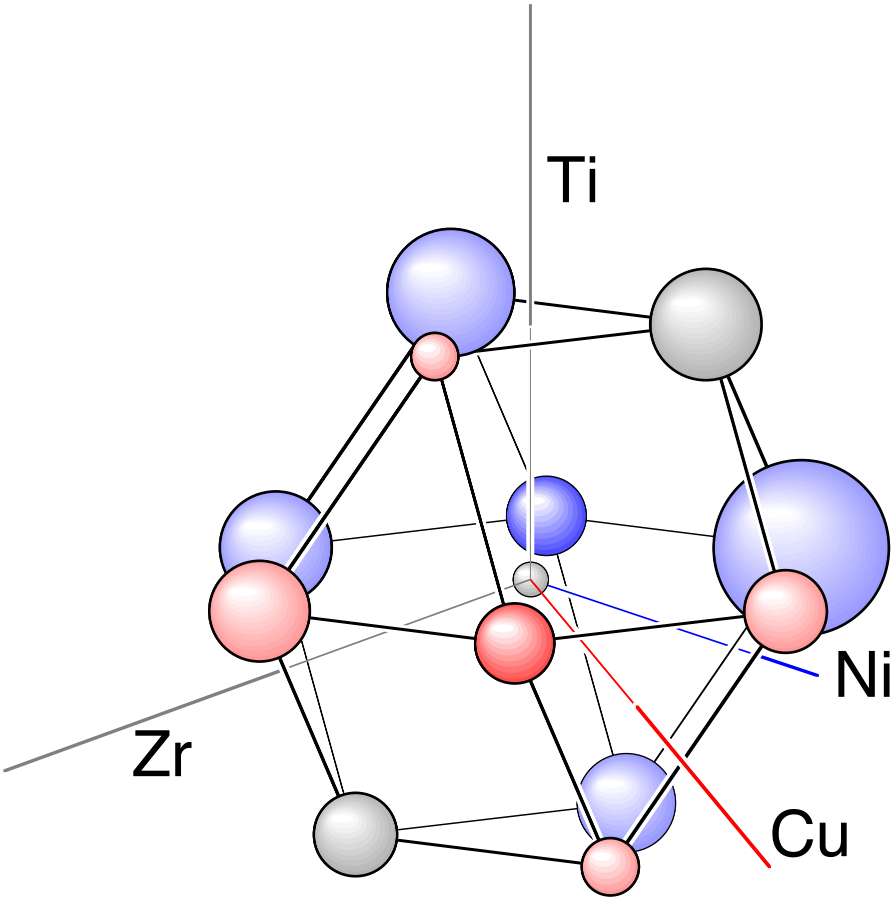

Figure 3.4: variation of critical casting thickness with composition

Projection of 12 compositions, located on the vertices of a cuboctahedron centered on Vit101 in the three-dimensional Cu-Ni-Ti-Zr composition space. For each of the compositions, a circle is drawn whose size is proportional to the critical casting thickness of that composition (cfr. Table 3.1). The color code reinforces the depth cues corresponding to the Cu-Ni axis.

forming ability than other directions. More compositions would need to be studied in order to form a more complete picture of the composition dependence of the glass forming ability in this alloy system.

3.2. SEM

Some of the samples used for optical microscopy were also examined in an SEM. Fig. 3.5 shows some of the spherical features in a backscattered electron image. To make the spherical features visible, the gain control was set to the maximum. Even then the spherical features are barely visible. No internal structure is discernible inside the sphere. Since the backscattered electron image is sensitive to composition changes*, this indicates that to within the resolution of the

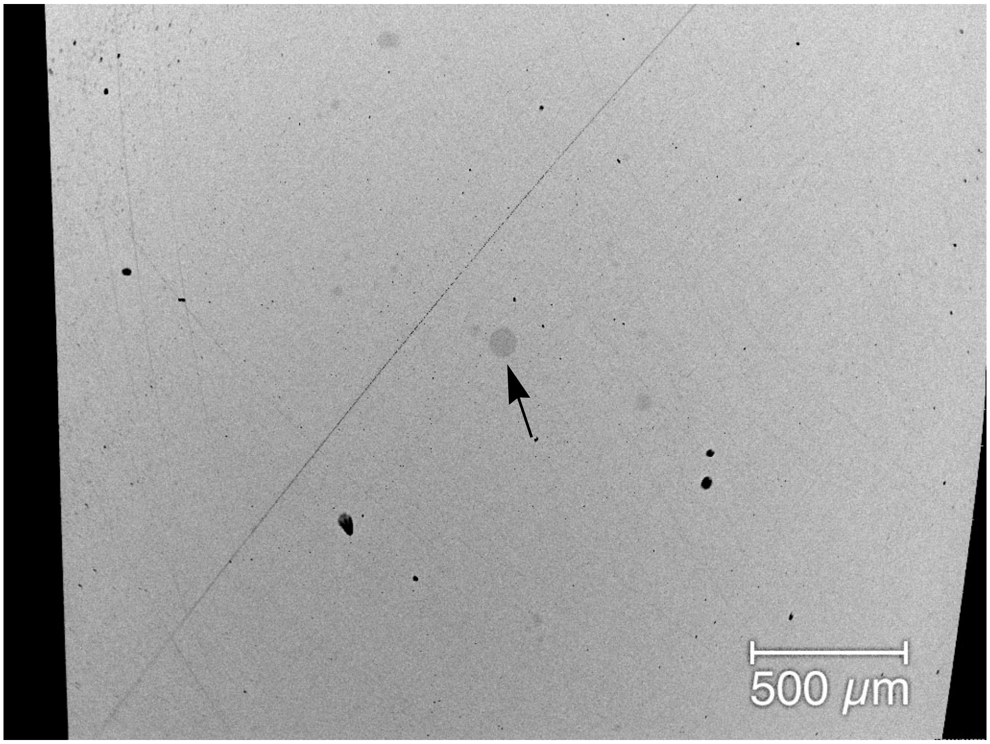

Figure 3.5: SEM micrograph of $Cu_{46}Ni_8Ti_{35}Zr_{11}$ wedge

The arrow points to one of the spherical features.

---

* The backscattered electron intensity is related to the average square of the atomic number of the sample. As such, the backscattered electron image for Vit101 and related alloys corresponds to a map of variations in the Zr content of the alloy.

instrument, the composition of the spheres is spatially uniform. The microprobe capability of the instrument was also used to look for any composition difference between the spheres and the surrounding material. Again, the composition was found to be uniform.

For comparison, Fig. 3.6 shows a sample with a smaller critical casting thickness, near the base of the wedge, where it is nearly fully crystallized. Here the microstructure is readily apparent in the backscattered electron image, without increasing the gain.

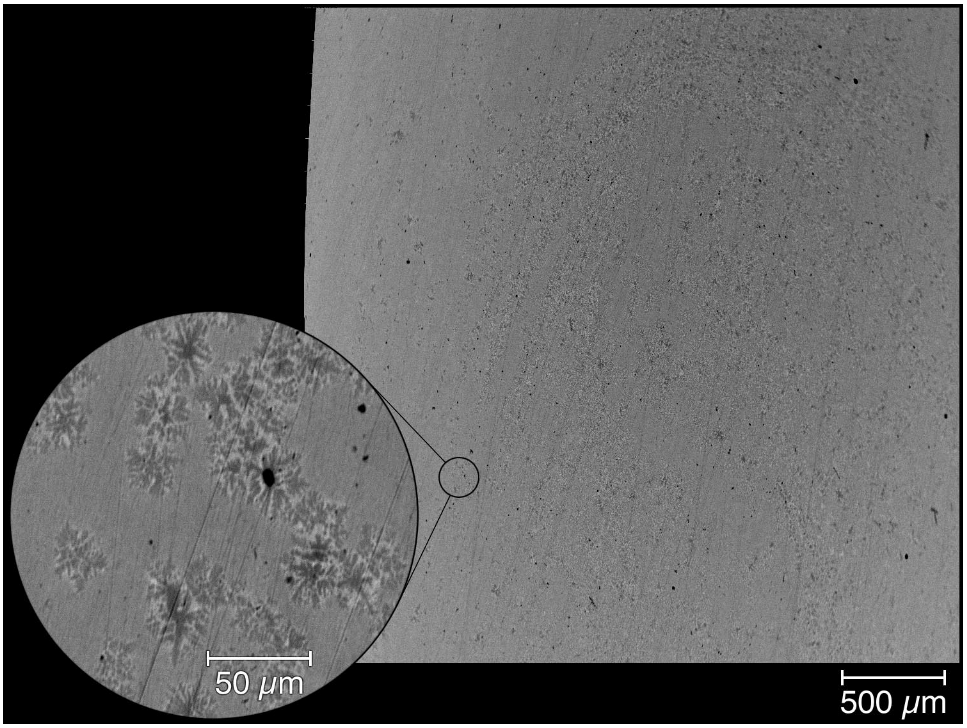

Figure 3.6: SEM micrograph of crystallized $Cu_{48}Ni_8Ti_{33}Zr_{11}$ *alloy*

3.3. X-ray diffraction

Diffraction patterns obtained from sections perpendicular to the long axis of the wedge-shaped samples at various thicknesses are shown in Fig. 3.7. These slices contain material that was cooled at a variety of cooling rates, ranging from very high cooling rates at the sample surface to a minimum cooling rate which depends on the thickness of the wedge at that point.

The diffraction pattern from the tip of the sample is a typical diffraction pattern for an amorphous material [21], showing two broad maxima. The diffraction pattern from the slice at 3 mm thickness is indistinguishable from the first. From 3 to 4 mm thickness the broad maximum from the amorphous diffraction pattern gradually becomes sharper. Comparing this change in shape with the patterns from >4 mm, it can be attributed to an emerging crystalline pattern superimposed on the amorphous background[*].

The peaks in the crystalline pattern are significantly broadened, which makes them harder to detect against the amorphous background. This peak broadening could be due to, e.g., an inhomogeneous strain distribution in the crystals or to the effect of small crystallite size [22].

When the diffraction patterns are compared with the micrographs from the same thickness, the spherical features are found to appear in the optical and SEM

---

[*] The amorphous background comes from the edges of the slice, which experienced a higher cooling rate than the center.

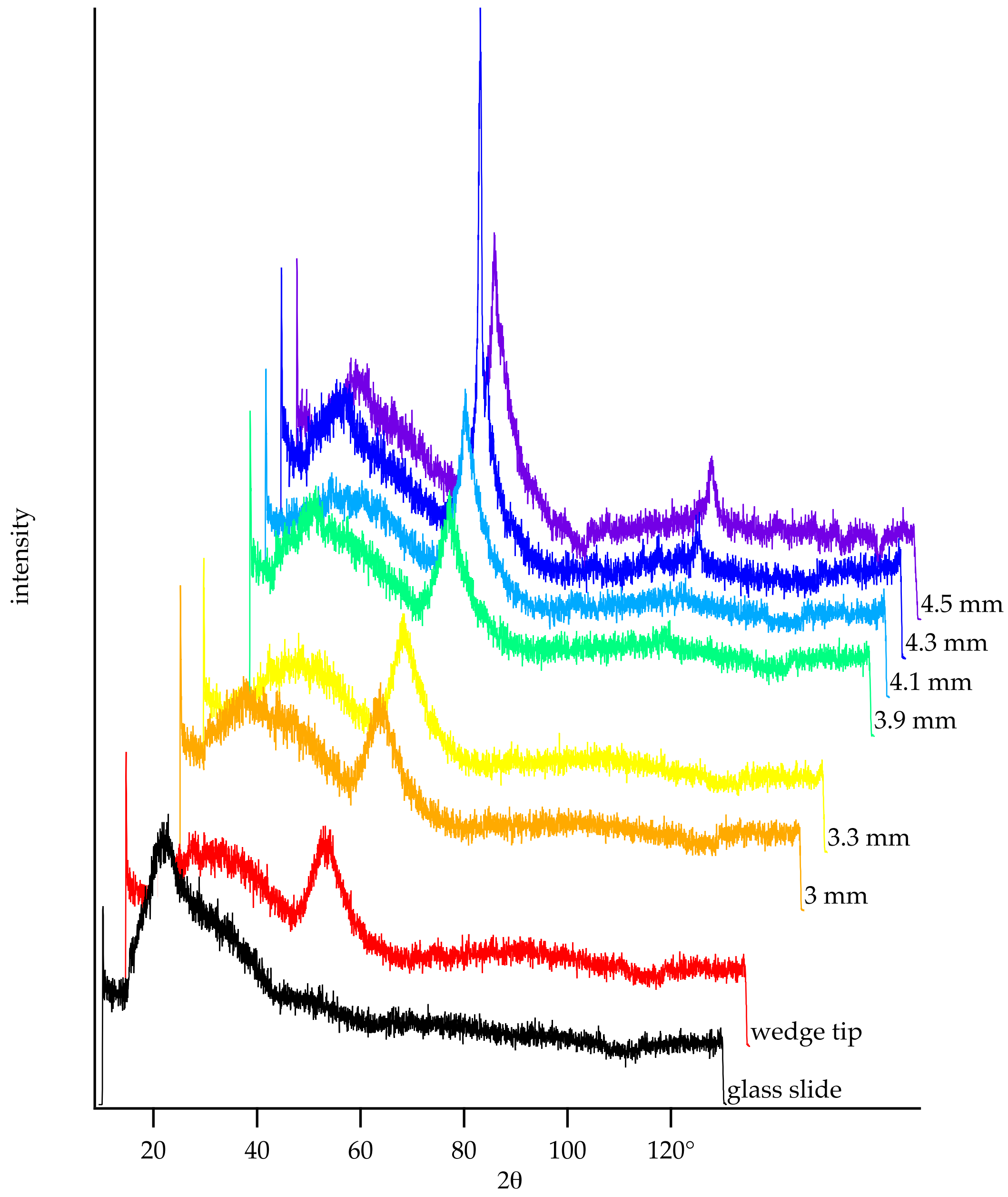

Figure 3.7: variation of X-ray diffraction pattern with thickness

X-ray diffraction patterns from a series of slices of a $Cu_{48}Ni_8Ti_{34}Zr_{10}$ *wedge. The background signal obtained with only the glass slide used for supporting the samples is also displayed. The indicated thickness is the thickness of the wedge where the slice was taken.*

micrographs at smaller thicknesses than the crystalline peaks in the diffraction pattern. The crystalline peaks are clearly distinguishable only when the spherical features are so large and closely spaced that they merge together. The size of the spherical features is also far too large to account for any significant peak broadening under the assumption that the crystallite size is the size of the spheres. In combination with the lack of any composition variation inside the spheres or between the spheres and the surrounding material —while crystals are expected to form only at compositions different from the nominal composition of the alloy— this makes it unlikely that the spherical features are individual crystals.

3.4. TEM

To further characterize the microstructure in the as-cast alloys with higher spatial resolution, a few alloys were studied by transmission electron microscopy. The TEM samples were prepared by ultramicrotomy. There are some artefacts, such as streaks and holes, visible in the micrographs, which are a consequence of this preparation technique.

The sample for the TEM micrograph in Fig. 3.8 was taken from a part of the wedge where spherical features appear in the optical micrographs. The sample preparation started from the unpolished half of the sample. Since the features can not be distinguished on an unpolished surface, the location where this sample was taken, relative to the features in the optical micrograph, is unknown. The sample could have come from inside one of the spheres, from the surrounding material, or from the interface between them.

Figure 3.8 shows a TEM dark field micrograph, with two very different microstructures separated by a sharp interface. Selected area diffraction (SAD) patterns corresponding to each of the regions are also shown as insets.

The region in the lower left of the micrograph is characterized by a large density of distinguishable nanocrystals. The corresponding diffraction pattern also indicates a nanocrystalline microstructure; compared to that of a fully amorphous material, the first diffraction ring is sharper, the second diffuse ring has split into several rings in which individual diffraction spots start to appear, and a third ring has become visible.

The region in the upper right of the micrograph is comparatively featureless. Few, if any, nanocrystals are highlighted in that part of the sample under these dark field conditions. The diffraction pattern resembles that of an amorphous sample more closely than the one in the lower left, but still shows some of the signs of short range order mentioned above. The microstructure in the lower left of the micrograph is certainly coarser, with a much higher density of nanocrystals, so the distribution of nanocrystals can be said to be spatially localized.

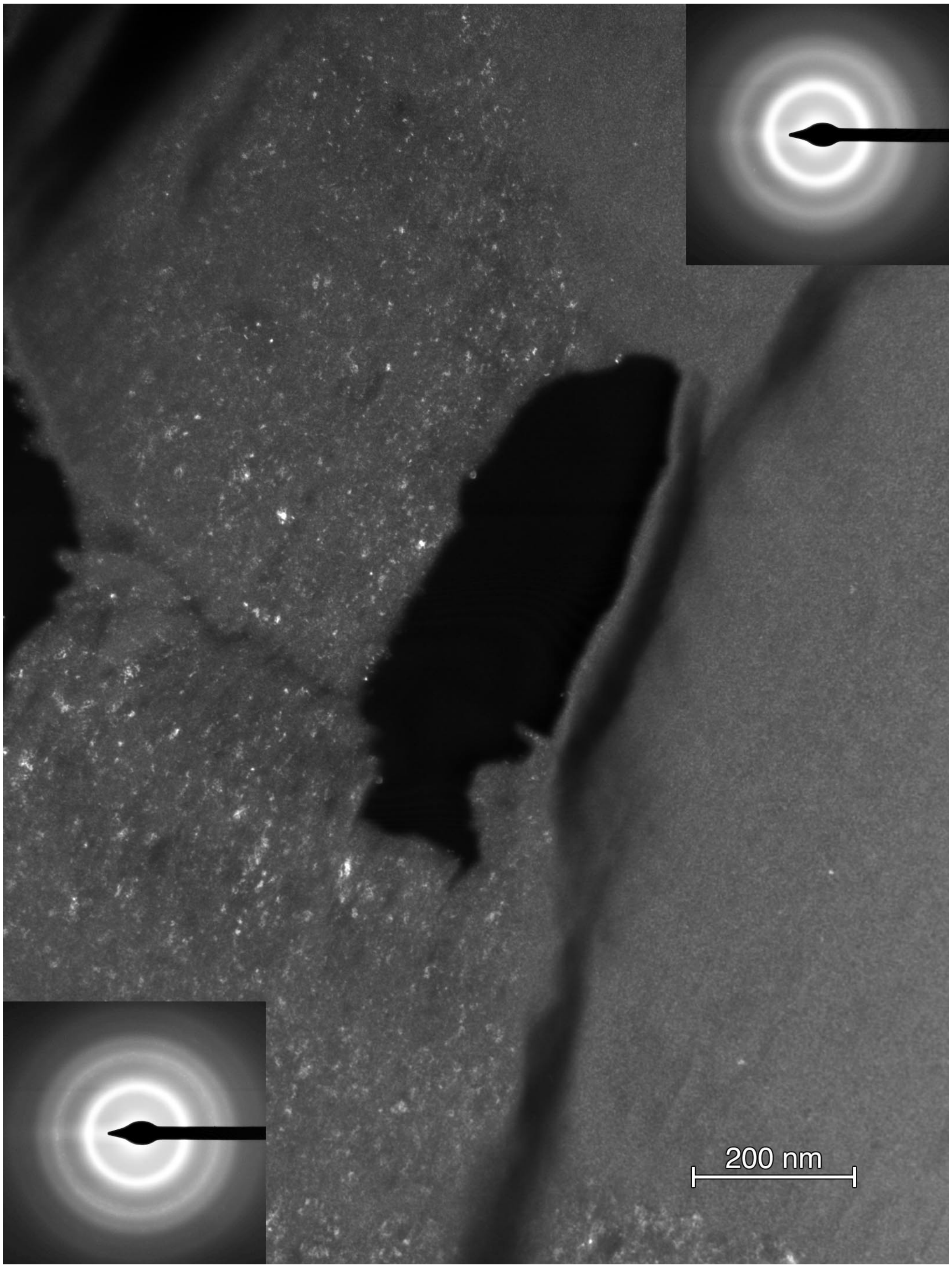

Figure 3.8: TEM micrograph of $Cu_{46}Ni_8Ti_{35}Zr_{11}$ sample with nanocrystals

Dark field electron micrograph and corresponding selected area diffraction patterns. This sample was taken from a wedge-shaped casting at 2 mm thickness.

3.5. Conclusions

The TEM micrograph shows that the distribution of nanocrystals in these samples is spatially localized. The other results can be explained as well, if the spheres in Fig. 3.1 and Fig. 3.2 correspond to the regions with a high density of nanocrystals. The contrast in the optical micrographs could be due to a difference in optical properties or to different mechanical properties leading to different polishing behavior resulting in topographic contrast. In agreement with the observations by SEM, there would be no concentration changes on length scales large compared to the size of the nanocrystals. And the size effect would broaden X-ray diffraction peaks to the point where they are hardly detectable when superimposed on the pattern from the surrounding amorphous material. Thus, the ensemble of experimental results presented in this chapter suggests that crystallization near the critical cooling rate is locally enhanced in spherical regions which form a large number of nanocrystals.

4. Crystallization Kinetics

In the proposed microstructure, spherical features contain a much higher number density of crystals than the surrounding regions, even though they have the same composition and seemingly experienced the same temperature history. This is not the crystallization behavior expected on the basis of established theories. It is postulated that these features did not in fact experience the same temperature history as the surrounding regions, but mark the site of localized recalescence events.

This claim is supported by the linear stability analysis of a set of differential equations describing the heat flow problem coupled with crystal nucleation and growth kinetics. The derivation, under “Spatially localized nucleation” on page 47, relies only on the inclusion of the heat of crystallization in the heat flow problem and some general characteristics of the temperature dependence of the nucleation and growth rates. The latter are adequately described by classical nucleation and growth theories, and are not fundamentally changed in more sophisticated descriptions of crystallization behavior.

4.1. Classical nucleation and growth kinetics

Classical nucleation theory

In classical nucleation theory [23-26], it is postulated that the free energy of a nucleus consists of a negative term proportional to the volume of the nucleus and a positive term proportional to the interfacial area between the nucleus and the liquid: $\Delta G_\mathrm{f} = \frac{4}{3}\pi r^3 \Delta g_\mathrm{f} + 4\pi r^2 \sigma_\mathrm{sf}$ for a spherical nucleus of radius r. As a result, growth only lowers the free energy of a nucleus once it has surpassed the critical size $r^\ddagger = -2\sigma_\mathrm{sf}/\Delta g_\mathrm{f}$, corresponding to a free energy barrier $\Delta G^\ddagger = \frac{16\pi}{3}\frac{\sigma_\mathrm{sf}^3}{\Delta g_\mathrm{f}^2}$ for nucleation. With some loss of generality, the parameters Δg_f and σ_sf may be equated with the bulk values of the free energy difference per unit volume between solid and liquid and the interfacial tension between solid and liquid, respectively.

Heterogeneous nucleation can occur at the interface between the liquid and another phase, if the crystal wets the other phase. A critical nucleus can then be formed at the interface between the liquid and the other phase with a smaller number of atoms than in the bulk liquid. This results in a reduction of the free energy barrier for nucleation by a factor $f(\theta) = ((2 + \cos\theta)(1 - \cos\theta)^2)/4$, where θ is the wetting angle.

The free energy $\Delta G^{\ddagger}$ of a critical nucleus can be regarded as the activation energy for nucleation in an Arrhenius equation[*] for the steady-state nucleation rate I_{v}:

$$I_{\mathrm{v}} = A \exp\left(\frac{-\Delta G^{\ddagger}}{k_{\mathrm{B}} T}\right). \tag{4.1}$$

The kinetic prefactor A takes into account the number of potential sites for heterogeneous or homogeneous nucleation, as well as the temperature dependence of the mobility in the liquid.

The temperature dependence of the nucleation rate results from thermodynamic as well as kinetic factors. Above the liquidus temperature, the liquid is thermodynamically stable, so no crystals can form and the nucleation rate is zero. As the liquid is undercooled below the liquidus temperature, the thermodynamic driving force for crystallization increases, i.e., Δg_{f} becomes more negative. This reduces the nucleation barrier $\Delta G^{\ddagger}$, so that the nucleation rate increases. Close to the glass transition, however, the temperature dependence of the nucleation rate is dominated by the temperature dependence of the kinetic prefactor; the nucleation rate decreases again as the mobility in the liquid decreases rapidly with decreasing temperature.

In a first approximation, the thermodynamic driving force varies linearly with the undercooling below the liquidus temperature: $\Delta g_{\mathrm{f}} = \Delta S_{\mathrm{f}}(T - T_{\mathrm{liq}})$. The proportionality constant is the entropy of fusion $\Delta S_{\mathrm{f}} = \Delta H_{\mathrm{x}} / T_{\mathrm{liq}}$, where ΔH_{x} is

---

[*] This does not imply that the temperature dependence of the nucleation rate follows an Arrhenius law. The activation energy and the prefactor in this expression are strongly temperature dependent.

the enthalpy of fusion. The resulting expression for the free energy of a critical nucleus is:

$$\Delta G^{\ddagger} = \frac{16\pi}{3}\frac{\sigma_{\mathrm{sf}}^{3}}{\Delta H_{\mathrm{x}}^{2}(1 - T/T_{\mathrm{liq}})^{2}}. \tag{4.2}$$

Assuming that the relevant mobility for nucleation is proportional to the fluidity of the liquid*, the temperature dependence of the kinetic prefactor can be described by the Vogel-Fulcher equation for viscosity: $A(T) = A'/\eta(T)$ with

$$A' = \frac{Nk_{\mathrm{B}}T}{3\pi r_{\mathrm{at}}^{3}}, \tag{4.3}$$

where N is the number of potential nucleation sites and r_{at} is the atomic radius, and

$$\eta(T) = \eta_{\infty}\exp\left(\frac{DT_{\mathrm{VF}}}{T - T_{\mathrm{VF}}}\right), \tag{4.4}$$

where η_{∞} is the high temperature limit of the viscosity, D is the fragility index, and T_{VF} is the Vogel-Fulcher temperature.

---

* This may or may not be a good approximation. Viscous flow in bulk glass forming liquids involves cooperative motion of a large number of atoms. Crystal nucleation involves local rearrangements of atoms with respect to their nearest neighbors. It has been shown that at low temperatures the diffusivity of small atoms may be orders of magnitude faster than predicted on the basis of viscosity by the Stokes-Einstein relation [27]. Conversely, at high temperature the cooperative motion required for viscous flow may be hindered in the vicinity of a crystal, so that the mobility may be lower than expected on the basis of viscosity. Nevertheless, the mobility in the liquid changes by many orders of magnitude between the liquidus temperature and the glass transition temperature, and the Vogel-Fulcher equation provides a plausible description of that temperature dependence.

Substituting Eq. 4.2 and Eq. 4.4 into Eq. 4.1, the following expression for the steady state nucleation rate is obtained:

$$I_v = \frac{A'}{\eta_\infty}\exp\left(-\frac{DT_{VF}}{T-T_{VF}}\right)\exp\left(-\frac{16\pi}{3}\frac{1}{k_B T}\frac{\sigma_{sf}^3}{\Delta H_x^2(1-T/T_{liq})^2}\right). \tag{4.5}$$

The contributions of the thermodynamic driving force and of the kinetic prefactor to the temperature dependence of the nucleation rate are illustrated in Fig. 4.1.

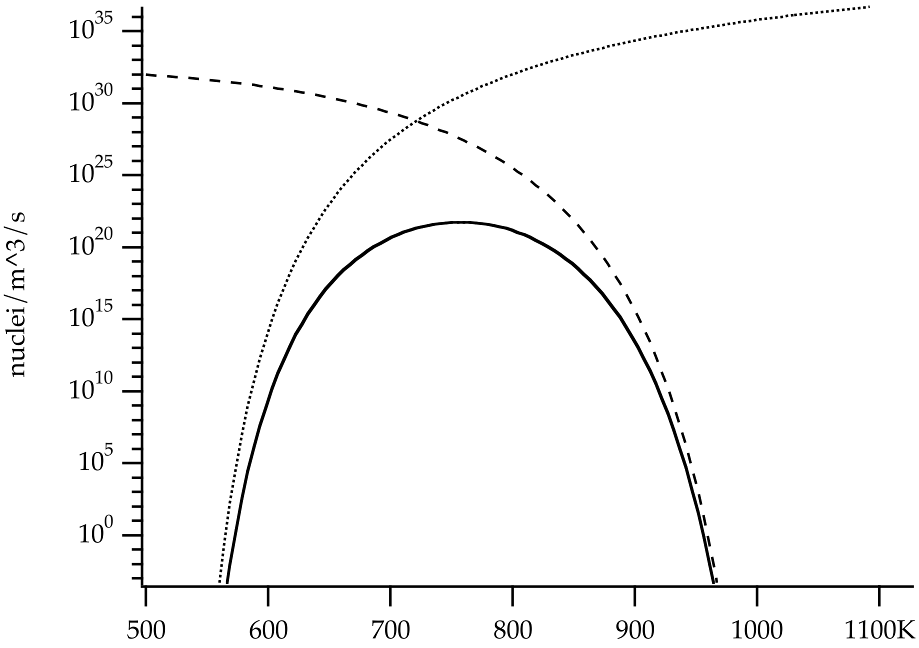

Figure 4.1: temperature dependence of nucleation rate

The dotted line illustrates the influence of the kinetic prefactor by using the heat of fusion instead of the temperature dependent thermodynamic driving force in the activation energy. The dashed line similarly illustrates the effect of the thermodynamic driving force by keeping the viscosity constant at its high temperature limit.

Validity of classical nucleation theory

Classical nucleation theory ignores several important aspects of nucleation in bulk metallic glass forming liquids. For example, it is implicitly assumed that crystallization is polymorphic, which is certainly not the case in Vit101. It is also questionable whether a description of the steady state nucleation rate is applicable to the instantaneous nucleation rate during continuous cooling. At best, classical nucleation theory provides a simplistic description of the complex process of nucleation in bulk metallic glass forming liquids.

It should be noted, however, that the nucleation rate varies over many orders of magnitude between the liquidus temperature and the glass transition temperature, and classical nucleation theory does capture the essential features of this temperature dependence. As a liquid is cooled from the melt, the nucleation rate initially increases with increased undercooling below the liquidus temperature and then decreases again as the mobility in the liquid decreases. This is in agreement with experimentally determined TTT-diagrams (See "TTT-diagrams" on page 44).

Using a more sophisticated description of the nucleation process, e.g., taking into account transient effects or partitioning, is unjustified unless it results in improved agreement with experiments. The calculated classical nucleation rate depends sensitively on parameters like interfacial tension[*], which are not

---

[*] A reduction of the interfacial tension from 150 mJ to 140 mJ increases the calculated maximum nucleation rate in Vit101 by a factor of 200.

precisely known. As a result, there is a large uncertainty inherent in calculated nucleation rates, and the interfacial tension is usually treated as a fitting parameter. If the more sophisticated description introduces new parameters with similar uncertainty, the additional fit parameters may improve quantitative agreement with experimental data, but in a physically meaningless way.

Crystal growth rate

Using transition state rate theory, the crystal growth velocity u can be expressed as the rate at which atoms from the liquid impinge on the crystal liquid interface, multiplied by a thermodynamic “sticking coefficient”:

$$u = \frac{k}{\eta}\left(1 - \exp\left(\frac{-\Delta g_{\mathrm{f}}}{k_{\mathrm{B}}T}\right)\right). \tag{4.6}$$

Similarly to the nucleation rate, the temperature dependence of the crystal growth rate is explained by the competing effects of increasing thermodynamic driving force and decreasing mobility as the liquid is cooled below the liquidus temperature. Contrary to nucleation, crystal growth does not require significant undercooling below the liquidus temperature; the maximum growth rate occurs at higher temperature than the maximum nucleation rate.

As was the case for the classical nucleation rate, this expression is strictly valid only for polymorphic crystallization. If the crystallization is non-polymorphic, partitioning will cause the composition of the liquid at the crystal liquid interface to differ from that of the bulk liquid. This normally* has the effect of lowering the crystal growth rate. As a result, the crystal growth rate becomes coupled to a diffusion problem. Diffusion leads to a $r \propto \sqrt{D_{\mathrm{diff}} t}$ growth law where the crystal size is proportional to the square root of time rather than $r \propto ut$ where it is directly proportional to time. Thus, sooner or later, the interface always overtakes the composition gradient. As the crystal grows and the composition difference between the liquid at the interface and the bulk liquid builds up, mass transport then becomes the dominating factor in the crystal growth rate.

Partitioning, by reducing the growth rate at the crystal liquid interface, also favors dendritic growth [28]. In the case of dendritic growth, the relevant length scale for the mass transport is not the size of the crystal, but the radius of curvature at the dendrite tip, resulting in a scaling law $r \propto D_{\mathrm{diff}} t / r_{\mathrm{tip}}$, where the size of the dendrite is again directly proportional to time. This would indicate that smaller dendrites always grow faster, but the increased interfacial area of smaller dendrites decreases the thermodynamic driving force for the crystallization. The microstructure is dominated by the dendrite arm size whose balance of mass transport and interfacial area results in the highest growth rate.

In summary, the simple picture of crystal growth limited by the rate interface attachment is complicated by mass transport effects in the case of non-polymorphic crystallization. This has ramifications for the crystal growth

---

* Partitioning decreases the driving force for crystallization, unless the curvature of the Gibbs free energy with respect to composition is negative. However, when this is the case, the nucleation and growth rates are likely to be influenced by spinodal decomposition, so that the classical nucleation and growth rates are no longer applicable.

rate and for the resulting microstructure, but in each case the temperature dependence of the crystal growth rate is determined by the competing effects of thermodynamic driving force and mobility.

TTT-diagrams

Time-temperature transformation diagrams, or TTT-diagrams, are often used in metallurgy to represent the temperature dependence of transformation kinetics. They represent the time required for a transformation, when the transformation is carried out isothermally, as a function of the temperature. Conventionally, the temperature is drawn on the vertical axis. Ideally the transformation should occur isothermally. For bulk glass forming alloys with sufficiently low critical cooling rates it is possible to experimentally determine the TTT-diagram for crystallization [29]. An example is shown in Fig. 4.2.

The “nose-shape” of the TTT-diagram is in qualitative agreement with classical nucleation and growth theory. But other theories result in very similar shapes for the TTT-diagram. The nose shape is simply a manifestation of the competition between the thermodynamic driving force for crystallization and the mobility in the liquid. Any reasonable attempt to describe crystallization in the context of glass formation should include these two effects, and will therefore necessarily result in a similar TTT-diagram. Quantitative agreement between theory and the experimentally determined TTT-diagram is not necessarily meaningful, when adjustable parameters like the prefactor in the nucleation rate and the interfacial

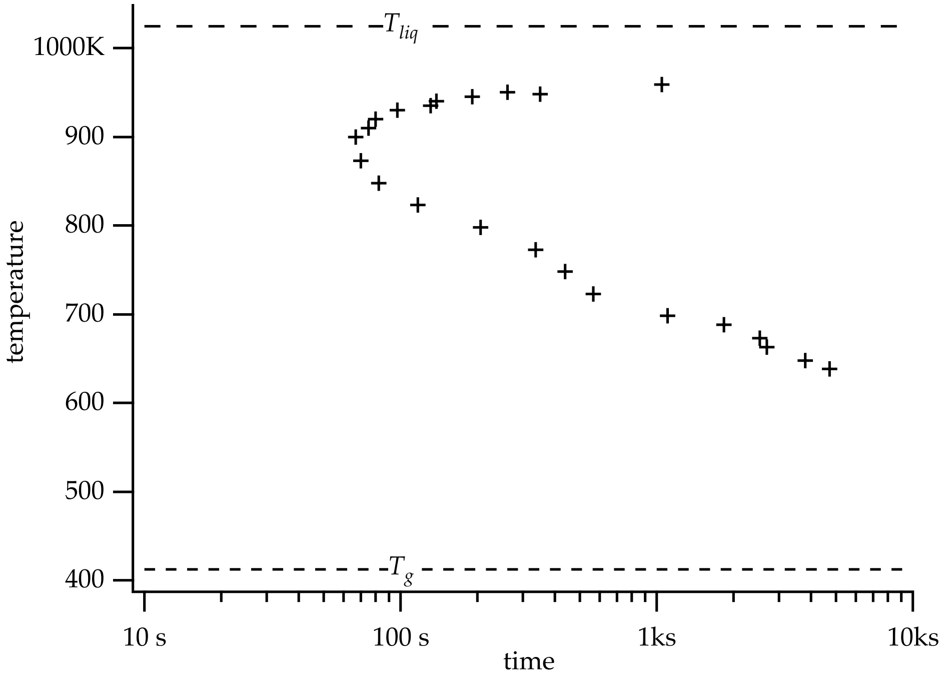

Figure 4.2: experimentally determined TTT-diagram

Time to onset of crystallization in graphite crucibles during isothermal experiments after cooling from the melt, vs. temperature of the isothermal segment, for $Zr_{41.2}Ti_{13.8}Cu_{12.5}Ni_{10}Be_{22.5}$ *(after Ref. [27]).*

tension can change the results by several orders of magnitude. The TTT-diagram is a useful characterization of the crystallization behavior for practical purposes, but it is not a good test to distinguish between various theoretical models.

Microstructure

A theoretical model of crystallization behavior should be judged not only on the accuracy with which it predicts crystallization kinetics, but also on its ability to explain the observed microstructures. The solidification microstructures of most metals and alloys can be interpreted in terms of classical nucleation and growth theory, if heterogeneous nucleation and segregation effects due to partitioning are included [30]. The temperature dependence of the mobility is insignificant in most alloys, but when it is included glass formation can also be explained. More specific mechanisms have been put forward to explain nanocrystalline microstructures in glass forming alloys, including quenched-in nuclei [31], phase separation prior to crystallization [32-34], and linked fluxes of interface attachment and diffusion [35].

However, the most striking aspect of the microstructure described in chapter 3 is that the spherical features contain a much higher number density of nanocrystals than the surrounding regions. Neither classical nucleation theory, nor any of the more specific mechanisms cited above, can explain such an inhomogeneous distribution of nuclei. In these theories, nucleation is considered to occur either at a heterogeneous nucleation site or randomly by a statistical fluctuation. To explain spatial localization of the nucleation rate, a feedback mechanism must be included to increase the likelihood of forming a nucleus in the vicinity of a previously nucleated crystal. The heat of crystallization released by a growing crystal can give rise to such a feedback mechanism. If the nucleation rate increases with temperature, then recalescence causes more crystals to form.

4.2. Spatially localized nucleation

Recalescence usually has the effect of creating fewer crystals: the heat release associated with crystal growth raises the temperature of the surrounding liquid, decreasing the nucleation rate. But in deeply undercooled liquids, i.e., on the “lower” branch of the TTT-diagram, the temperature dependence of the mobility in the liquid overshadows the temperature dependence arising from the free energy barrier for nucleation, so that the nucleation rate increases with increasing temperature. This sign change in the temperature dependence of the nucleation rate changes the nature of the recalescence instability.

Differential equations for nucleation and growth

To include the effect of the heat of crystallization, which is responsible for recalescence, in the heat flow equation, a heat release term proportional to the volume growth rate $\partial X / \partial t$ of the crystals is added in Eq. 4.7.a. This term couples the crystallization behavior, described by nucleation in Eq. 4.7.b and growth in Eq. 4.7.c, to the heat flow problem.

$$\frac{\partial T}{\partial t} = \alpha \nabla^2 T + \frac{\Delta H_x}{c_p} \frac{\partial X}{\partial t} \qquad (4.7.a)$$

$$\frac{\partial N}{\partial t} = I_v(T) \qquad (4.7.b)$$

$$\frac{\partial X}{\partial t} = \langle \dot{V}_x \rangle(T) N \qquad (4.7.c)$$

T, N and X are temperature, number density of crystals and volume fraction crystallized, respectively. These variables are dependent on time and spatial position. The parameters thermal diffusivity α, heat of crystallization per unit volume ΔH_x, and heat capacity c_p are roughly constant, while the nucleation rate I_v is temperature dependent. The details of crystal growth kinetics are lumped together in the average volume growth rate $\langle \dot{V}_x \rangle$ of the crystals, which depends on the size distribution of the crystals as well as temperature.

Linear stability analysis

By linearizing these equations around a solution T^0, N^0, X^0 at an arbitrary point in time t^0, and using the spectral representation of the Laplacian*, a set of linear ordinary differential equations with constant coefficients is obtained for each of the terms in the spectral representation:

$$\frac{\partial T_i^1}{\partial t} = -\alpha k_i^2 T_i^1 + \frac{\Delta H_x}{c_p} \frac{\partial X_i^1}{\partial t} \tag{4.8.a}$$

$$\frac{\partial N_i^1}{\partial t} = I_v'(T^0) T_i^1 \tag{4.8.b}$$

$$\frac{\partial X_i^1}{\partial t} = \langle \dot{V}_x \rangle'(T^0) T_i^1 N_i^0 + \langle \dot{V}_x \rangle (T^0) N_i^1 \tag{4.8.c}$$

---

* The spectral representation of a linear operator amounts to a projection onto the eigenfunctions of the operator. See "Solutions to the Fourier heat flow equation" on page 75.

$I_v'(T^0)$ and $\langle \dot{V}_x \rangle'(T^0)$ are the temperature derivatives, evaluated at T^0, of the nucleation and growth rates $I_v(T)$ and $\langle \dot{V}_x \rangle(T)$, respectively. The superscript 1 refers to the deviation from the original solution with superscript 0. The subscript i refers to the i^{th} term in the spectral representation of the Laplacian, with eigenvalue $-k_i^2$. In the case of rectangular boundary conditions for example, the eigenfunctions of the Laplacian are the terms in a Fourier series, e.g., for temperature $T(x, y, z, t) = T^0 + \sum T^1_{k_x, k_y, k_z}(t) \sin(k_x x) \sin(k_y x) \sin(k_z x)$, indexed by three wavenumbers k_x, k_y, k_z, with $k^2 = k_x^2 + k_y^2 + k_z^2$.

The stability of the original solution is determined by the eigenvalues

$$\lambda_0 = 0 \text{ and } \lambda_\pm = \frac{1}{2}\left(\delta \pm \sqrt{\delta^2 + 4\frac{\Delta H_x}{c_p} I_v' \langle \dot{V}_x \rangle}\right), \text{ with } \delta = -\alpha k_i^2 + \frac{\Delta H_x}{c_p} \langle \dot{V}_x \rangle' N_i^0 . \quad (4.9)$$

If the real part of any of the eigenvalues is positive, deviations from the solution T^0, N^0, X^0 will grow exponentially. The eigenvalue λ_0 corresponds to an eigenvector involving only the number density of nuclei, and is not relevant to the recalescence instability.

Normal recalescence

In the normal case, where the nucleation rate decreases with increasing temperature, the second term under the square root is negative, so the square root is either real and smaller than δ or imaginary. Therefore, the sign of the real part of the eigenvalues is the sign of δ, so the stability of the solution is determined only by the sign of δ. In the early stages of the crystallization process, the number density of nuclei N^0 is small, so δ is dominated by the thermal conductivity term $-\alpha k_i^2$ in Eq. 4.9, which is always negative. As the number of crystals increases, the heat release term contributes more to δ, eventually making δ positive if the growth rate increases with temperature. The first mode in the series expansion becomes unstable when $N_1^0 = \alpha\left(\frac{2\pi}{L}\right)^2 \frac{c_p}{\Delta H_x \langle \dot{V}_x \rangle}$, where L is the thickness of the sample. This is the well-known recalescence phenomenon: the liquid is undercooled until sufficient nuclei are formed, at which point a rapid increase in temperature is observed. This type of recalescence instability (type I in Fig. 4.3) only occurs in the late stages of crystallization, when a sufficiently large number of nuclei have formed. If heterogeneous nucleation prevents significant undercooling or if the thermal conductivity is sufficiently high, the sample is fully crystallized before the instability occurs, and recalescence is not observed.

Localized recalescence

If the nucleation rate increases with increasing temperature, however, a second type of recalescence instability (type II in Fig. 4.3) occurs. In this case, the second term under the square root is positive, so the square root is real and greater than δ. Therefore, λ_+ is always positive, and the solution is always unstable. This means that, even in the early stages of crystallization, the solution is sensitive to any spatially varying perturbations in temperature or composition of the original melt, or the random but discrete distribution of nuclei. Qualitatively speaking, the nonlinearities of the equations are such that positive deviations are amplified more than negative deviations, and there is a coupling in the nucleation and

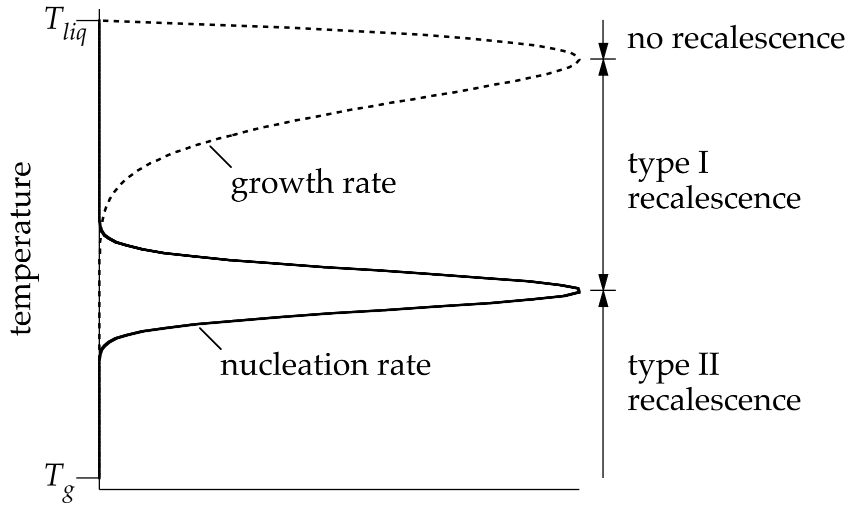

Figure 4.3: temperature regimes for type I and type II recalescence

> *Type I is the normal recalescence instability which occurs in the late stages of crystallization. It occurs when the growth rate (dashed line) increases with temperature and the nucleation rate (solid line) decreases with temperature. Type II recalescence occurs only in deeply undercooled liquids, where both the nucleation and growth rate increase with temperature. This instability exists even in the early stages of crystallization and is spatially localized.*

growth terms of the shorter wavelength modes to the amplitude of longer wavelength temperature modes centered on the same position. The result of the instability is that a small, point-like heat source —e.g., a growing crystallite— leads to localized increases in temperature, nucleation rate, and growth rate, which grow exponentially in size and amplitude over time. It is proposed that the spherical clusters of nanocrystals reported in this work are the manifestation of such localized recalescence phenomena.

The time required for the instability to manifest itself is the inverse of the positive eigenvalue λ_+. Using classical nucleation theory for the homogeneous nucleation rate (Eq. 4.5), with an interfacial tension of $100\mathrm{mJ/m^2}$, the maximum temperature derivative of the nucleation rate in Vit101 is $3\times10^{26}\mathrm{nuclei/m^3sK}$. The heat capacity, heat of crystallization and thermal diffusivity of Vit101 have been measured as $45\mathrm{J/mol\,K}$, $11.3\mathrm{kJ/mol}$ and $5\times10^{-6}\mathrm{m^2/s}$, respectively [36,37]. The crystal growth rate can be estimated at $6\times10^{-26}\mathrm{m^3/s}$ from the typical size of the nanocrystals in Fig. 3.8 (10 nm) and the time they had to grow (not more than 1 s). With those values, the time constant for a feature size of 200 μm evaluates to 250 ms. Considering that the timescale for cooling the liquid to form a glass is on the order of seconds in this alloy, this implies that the predicted recalescence instability is significant in the crystallization kinetics of Vit101 during glass formation.

Glass formation

In the process of glass formation, it is inevitable to pass through the deeply undercooled liquid regime where the nucleation rate increases with temperature, and encounter the type II recalescence instability. The effect of the recalescence is to increase the size and number of crystals formed at a given external cooling rate, increasing the critical cooling rate for glass formation. Furthermore, the localized heat release from the few crystals which were nucleated and had the opportunity to grow at high temperature —before the recalescence instability existed— causes the recalescence to occur locally. At cooling rates above the critical cooling rate the recalescence is quenched by the surrounding liquid. As the cooling rate decreases, the number and size of crystals nucleated at high temperature increases, and there is more time for thermal conduction, so the localized recalescence events are more closely spaced and grow to greater size, eventually overlapping. The overlap reduces heat flow to the surrounding liquid, resulting in mutual enhancement of the recalescence events. When the heat flow is insufficient to quench a recalescence event, this recalescence event continues to grow, engulfing the surrounding recalescence events, and ultimately leading to complete crystallization.

In this proposed crystallization mechanism it is the interaction of the localized recalescence events that triggers complete crystallization of the sample. Without the interaction or the localized recalescence events, the transition from glass formation to crystallization would be much more gradual, with a wide range of cooling rates where partial crystallization is observed. The critical cooling rate for glass formation would be lower, and not so well-defined. In isothermal experiments too, recalescence causes the onset of crystallization to be sharper than it would be without recalescence (type I recalescence can be compensated for in a temperature-controlled experiment, but the localized type II recalescence can not). In general, crystallization kinetics in this proposed crystallization mechanism are characterized by an incubation time, where the amplitude and size of the localized recalescence events are too small to be detected, followed by rapid crystallization when the recalescence involves the entire sample.

5. Alloy Development

5.1. Requirements for glass formation

One of the reasons for studying the crystallization behavior of bulk glass forming alloys is to use the knowledge so obtained in the search for new and improved glass forming alloys. In this regard, the details of the crystallization kinetics are of less interest than the composition dependence of the critical cooling rate. Based on the discussion of crystal nucleation and growth kinetics in the previous chapter, some general statements can be made about the requirements for a good glass forming composition.

High reduced glass transition temperature

The reduced glass transition temperature $T_{rg} = T_g/T_{liq}$ plays a crucial role in determining the glass forming ability of an alloy. To make a glass, the alloy must be cooled from the thermodynamically stable liquid above the liquidus temperature to below the glass transition temperature. The reduced glass transition temperature not only gives the width of this temperature interval, it also determines how close to the liquidus temperature the decreasing mobility in the liquid starts to reduce the nucleation rate.

A high reduced glass transition temperature therefore leads to low nucleation rates. If the reduced glass transition temperature is above 2/3, the rate of homogeneous nucleation is so low that it is negligible at laboratory time scales [24].

Variations in the reduced glass transition temperature are largely due to the variations in the liquidus temperature. The glass transition temperature scales roughly with the binding energy of the alloy, and does not depend strongly on composition [38]. The search for good glass forming alloys therefore starts with low-lying liquidus surfaces, i.e., near deep eutectics.

Shift away from phases that nucleate easily

The eutectic indicates which liquid composition is most stable compared to the competing crystalline phases under thermodynamic equilibrium conditions, i.e., at infinitely slow cooling rates. At finite cooling rates most liquids can be undercooled significantly below their liquidus temperature before crystallization sets in. The degree to which the liquid can be undercooled depends on the cooling rate and the nucleation kinetics. At the critical cooling rate, the undercooling diverges and the liquid can be undercooled to any temperature without crystallizing.

If competing crystalline phases have different interfacial tensions with the liquid, the degree to which they can be undercooled below their respective liquidus temperatures will differ. Phases for which the interfacial tension with the liquid is low can nucleate more easily, and will exhibit less undercooling, than those for which the interfacial tension is higher [39].

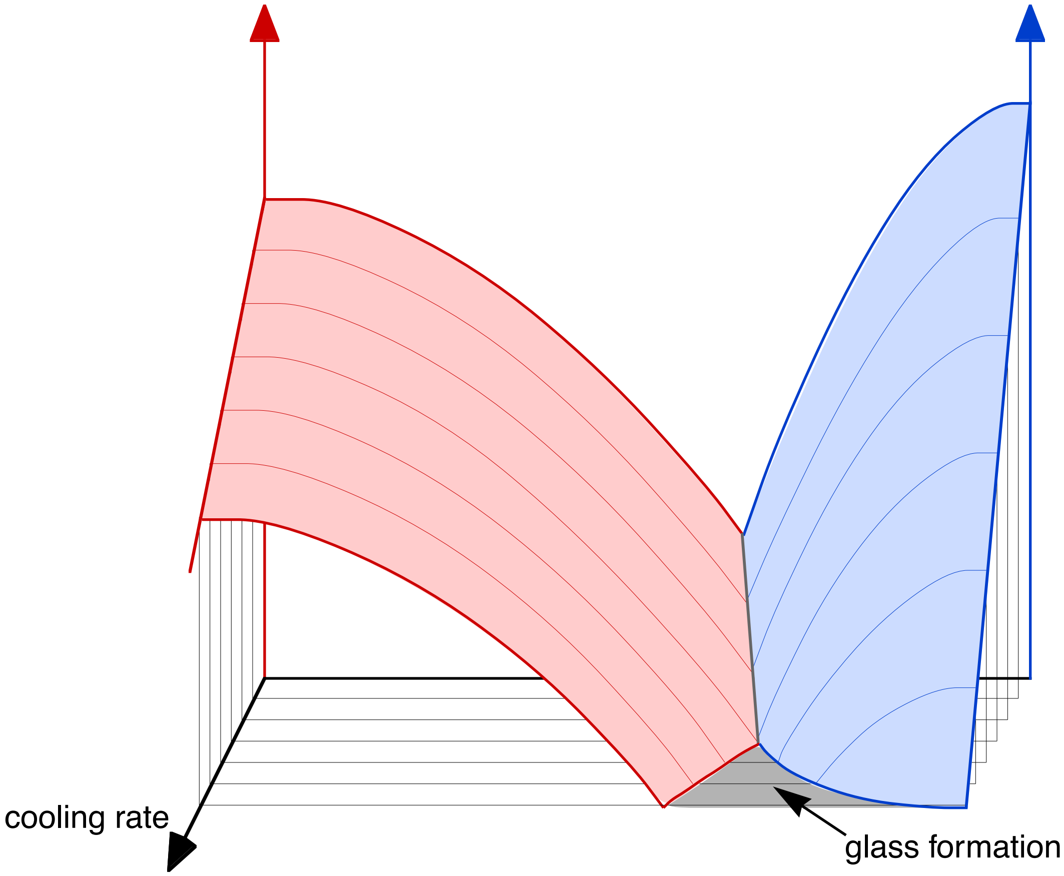

Figure 5.1: schematic non-equilibrium phase diagram of eutectic system

> *The liquidus curves in this phase diagram are shifted to lower temperatures to account for the undercooling that occurs at finite cooling rates. Glass formation occurs when the undercooling reaches the glass transition. The composition which forms a glass at the lowest cooling rate is shifted, relative to the eutectic composition, towards the phase with higher undercooling.*

The relevance of this effect for glass formation and its composition dependence is illustrated in Fig. 5.1. As the cooling rate increases, the "non-equilibrium eutectic" composition shifts away from the phases that exhibit less undercooling towards those that can be undercooled more. The glass forming composition at the lowest cooling rate where glass formation occurs, i.e., by definition the best glass forming composition, is this “non-equilibrium eutectic” at that cooling rate.

The interfacial tension with the liquid is expected to be highest for simple crystal structures, and lowest for topologically close-packed structures whose local structure resembles that of the liquid [40].

Avoid heterogeneous nucleation

The resistance to crystallization of glass forming alloys depends at least partly on the lack of homogeneous nucleation at high temperatures, where the crystal growth rate is high. Heterogeneous nucleation sites increase the nucleation rate, particularly at high temperatures, and are therefore deleterious to glass forming ability. The effect of processing conditions —e.g., the use of a fluxing agent, choice of atmosphere and crucible material, impurities in the alloying elements, and general cleanliness of the apparatus— on glass forming ability of the alloy can be explained by their effect on heterogeneous nucleation.

The use of a fluxing agent is of particular interest. For some bulk glass forming alloys, notably those in the Pd-Ni-P family, the glass forming ability is greatly improved by the use of a flux [41], boron oxide in the case of Pd-Ni-P. The effect of the boron oxide flux in improving the glass forming ability of Pd-Ni-P is generally attributed to the removal of heterogeneous nucleation sites from the melt and their dissolution in the liquid boron oxide flux.

The role of oxygen impurities has also been studied. Deliberate contamination of $Zr_{52.5}Ti_5Cu_{17.9}Ni_{14.6}Al_{10}$ was found to cause crystallization at shorter times and higher temperatures [42]. Throughout this work, particular care was taken to keep the oxygen contamination level as low as possible.

Low mobility

To the extent that the glass transition temperature characterizes the mobility of the liquid, the requirement of low mobility coincides with the requirement of a high reduced glass transition. For some liquids, however, the mobility increase above the glass transition is much more gradual than for others. According to Angell [43], supercooled liquids can be classified as strong or fragile on the basis of the temperature dependence, scaled to the glass transition temperature, of their viscosity. In this context strong liquids, which have lower mobility, are expected to be better glass formers.

Applying this principle to alloy development is impractical, because determining the temperature dependence of the viscosity of an alloy requires extensive characterization. It is far simpler to measure the glass forming ability directly.

Control phase separation

The effect of phase separation on glass forming ability is ambiguous. Phase separation could in principle be beneficial for glass formation, by inhibiting crystal growth and necessitating more nucleation; if crystals nucleated in one of the decomposed phases do not grow into the other decomposed phase, separate crystals need to be nucleated in each of the decomposed regions. Phase separation may not affect glass forming ability at all, if the critical cooling rate is limited by a process that occurs before phase separation occurs. But phase separation could easily ruin the glass forming ability of an alloy: in all likelihood, at least one of the two complementary composition shifts involved in phase separation is towards a poorer glass forming composition.

Whether its effects are desired or undesired, if phase separation affects the glass forming ability of an alloy, the composition dependence of the crystallization behavior is complicated by the fact that the composition is no longer spatially uniform and changes over time. Straightforward assumptions about the effects of composition changes on crystallization behavior, e.g., that changing the composition away from a crystalline phase disrupts the crystallization of that phase, break down. So if phase separation plays a part in the crystallization behavior of an alloy, it is important to recognize that fact to avoid drawing the wrong conclusions.

5.2. Empirical optimization

The object of alloy development is to minimize some cost function defined on a composition space. The cost function represents the trade-off between the various properties that are desired or undesired for the alloy. In order for the optimization to be mathematically meaningful the cost function must be scalar, so that an ordering relation is defined. In the context of bulk metallic glasses, the cost function to be optimized is the inverse of the glass forming ability.

Physical insight and theoretical predictions can be invaluable aids for this optimization problem, by suggesting promising starting points and by interpreting and extrapolating measured data. But at some point the properties must be measured for a number of alloy compositions to verify or determine experimentally which composition is most desirable. These measurements are often time consuming and expensive, so it is worthwhile to choose an optimization algorithm that keeps the number of measurements to a minimum.

Brute force

Conceptually, the optimal composition in an alloy system is determined by measuring every possible composition and choosing the one that gave the best result. In practice, only a finite number of measurements can be performed. Still, a brute force approach, where a large number of samples spanning the entire composition space is measured, is always an option. In fact, while other methods may be more efficient at finding a local optimum, without a priori knowledge about the function to be optimized a brute force search is the only method certain to find a global optimum.

According to the Nyquist sampling theorem [44], the minimum feature size that is certain to be detected is twice the spacing between the samples. The number of samples required for a brute force search is therefore inversely proportional to the

N^{th} power of the minimum feature size, where N is the dimensionality of the space to be searched. Since the dimensionality of the composition space for an n-component system is $n - 1$, this number rapidly becomes prohibitively large[*] as the number of components increases. The brute force approach is appropriate only if the space to be searched is small, if the measurements are quick and cheap, or if all other options have been exhausted. Alloy development with multi-component alloys does not normally fall under any of these categories.

Steepest descent

Instead of attempting to measure the glass forming ability for every composition in an alloy system to find the best glass former, more efficient strategies proceed towards a local optimum by focusing on the directions in composition space in which the glass forming ability improves most rapidly. These strategies require some —ideally quantitative— information about the local composition dependence of the glass forming ability. When such information is not available directly from experiments and/or theory, the composition dependence can be approximated by linearly extrapolating from measurements on a small number of individual compositions, i.e., by determining the gradient.

---

[*] For example, there are more than 10000 compositions in a grid spaced at 5% composition intervals for a 5-component system. For a grid spaced at 1% intervals the number is approximately 1×10^{8}, and for a 5% grid in an 8-component system it is 3×10^{6}. In general, in an n-component system there are $\prod_{k=1}^{n-1}\frac{p+k}{k}$ compositions spaced at intervals of $\frac{1}{p}$ on a grid with the symmetry of the composition space.

The benefit that can be gained by using a steepest descent strategy for optimizing composition depends on the accuracy with which the composition dependence can be extrapolated, and on the complexity of the “glass forming ability landscape.” The difference in glass forming ability between the compositions used for the extrapolation must be larger than the uncertainty on the measurement, otherwise the resulting gradient is meaningless. This requirement imposes a lower bound on the composition difference between the alloys used for the extrapolation. On the other hand, the complexity of the landscape imposes an upper bound on the distance over which the gradient is accurate. A steepest descent strategy is most effective in simple landscapes, where little information is needed to specify the composition dependence of the glass forming ability.

Based on the correlation between glass forming ability and the reduced glass transition temperature, whose composition dependence follows that of the liquidus temperature, it is not unreasonable to expect the glass forming ability landscape to be rather similar to the liquidus surface in a eutectic phase diagram, illustrated in Fig. 5.2. In this analogy, the glass forming ability is limited by the primary crystallizing phase, and improves monotonically as the composition is shifted away from the composition of this crystalline phase until a different phase becomes the primary crystallizing phase. The landscape is then a smoothly varying surface, except where the surfaces for different primary crystallizing phases intersect, there the slope is discontinuous. A steepest descent strategy should work relatively well in such a landscape.

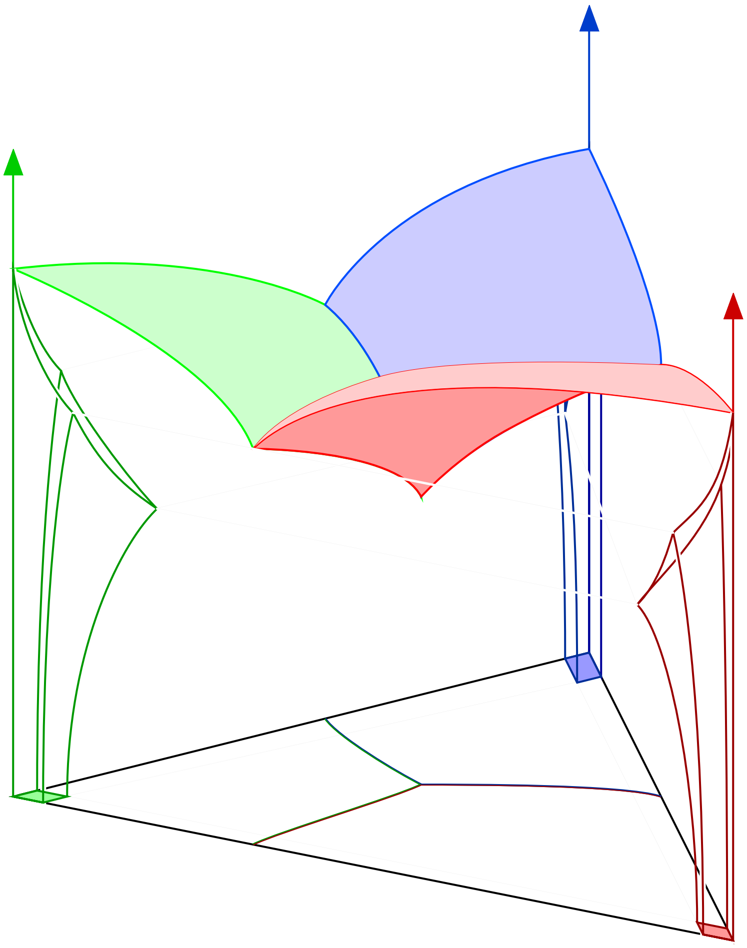

Figure 5.2: schematic illustration of ternary eutectic phase diagram

The liquidus projection is shown in the base plane.

Discussion

The results from Fig. 3.4 on page 27, however, are inconsistent with such a simple glass forming ability landscape. The critical casting thickness of Vit101 displays a local minimum in the middle of a good glass forming region, where a local maximum is expected. No explanation for this surprising result has been established yet. One possibility is that where there is a transition from one primary crystallizing phase to another, the crystallization of one phase is accelerated by the crystallization of the other phase. In the discussion leading up to “Spatially localized nucleation” on page 47, such feedback effects were put forward to explain the microstructure described in chapter 3. It is possible that the feedback effect results not purely from temperature dependence but also involves composition dependence and partitioning.

Whatever the cause of the unexpected result in Fig. 3.4, it clearly indicates that the glass forming ability landscape in the region of interest is complex, and contains features which were overlooked in the work of Lin [45], where compositions were spaced 2 to 5% apart. Figure 3.4 shows that the glass forming ability can change significantly with composition changes as small as 1%. The complexity of the landscape disrupts the steepest descent optimization strategy, while the small feature size drastically increases the number of samples required for a comprehensive brute force search. As yet, our understanding of the crystallization process —and knowledge of the thermodynamic properties— in these multicomponent bulk glass forming alloys is insufficient to predict the crystallization behavior at the level of detail required to move alloy development past empirical optimization.

6. Annealing

The stability against crystallization at temperatures slightly above the glass transition enables bulk metallic glasses to be processed more like plastics than like metals, for example by extrusion of amorphous powders [46]. Any discussion of crystallization behavior of metallic glasses is therefore incomplete if it does not address crystallization upon heating of amorphous samples.

6.1. Experimental results

Small angle X-ray scattering (SAXS)

The crystallization behavior of Vit101 samples during annealing was observed *in situ* by small angle X-ray scattering. The evolution of the radial average of the scattering intensity with time is shown in Fig. 6.1 and Fig. 6.2, for two different temperatures. The Q value on the horizontal axis in these plots is the modulus of the scattering vector. The as-prepared samples exhibit only surface scattering, which drops off rapidly at increasing Q and is insignificant for Q values greater than 0.05 Å. During annealing, the scattered intensity increases over time and an interference maximum develops at Q=0.073 Å^{-1} for the sample annealed at 665 K and at Q=0.036 Å^{-1} for the sample annealed at 769 K. In the sample annealed at the higher temperature, the signal changes shape as well, with a shoulder developing around Q=0.07 Å^{-1}.

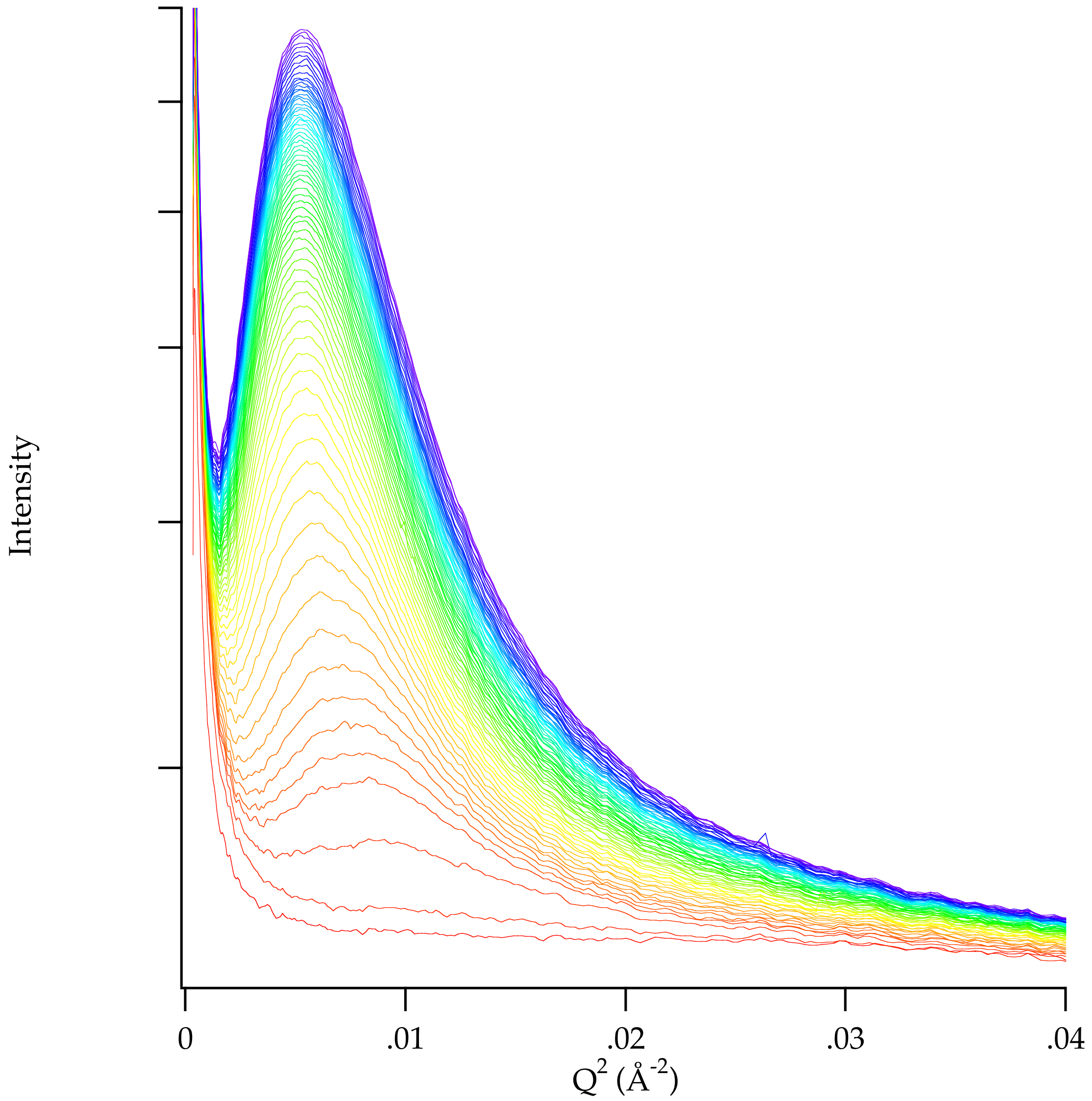

Figure 6.1: in situ SAXS data for Vit101 annealed at 665 K

Logarithm of the scattered intensity vs. Q^2.

The scattered intensity exhibits an interference maximum, and its amplitude increases with time.

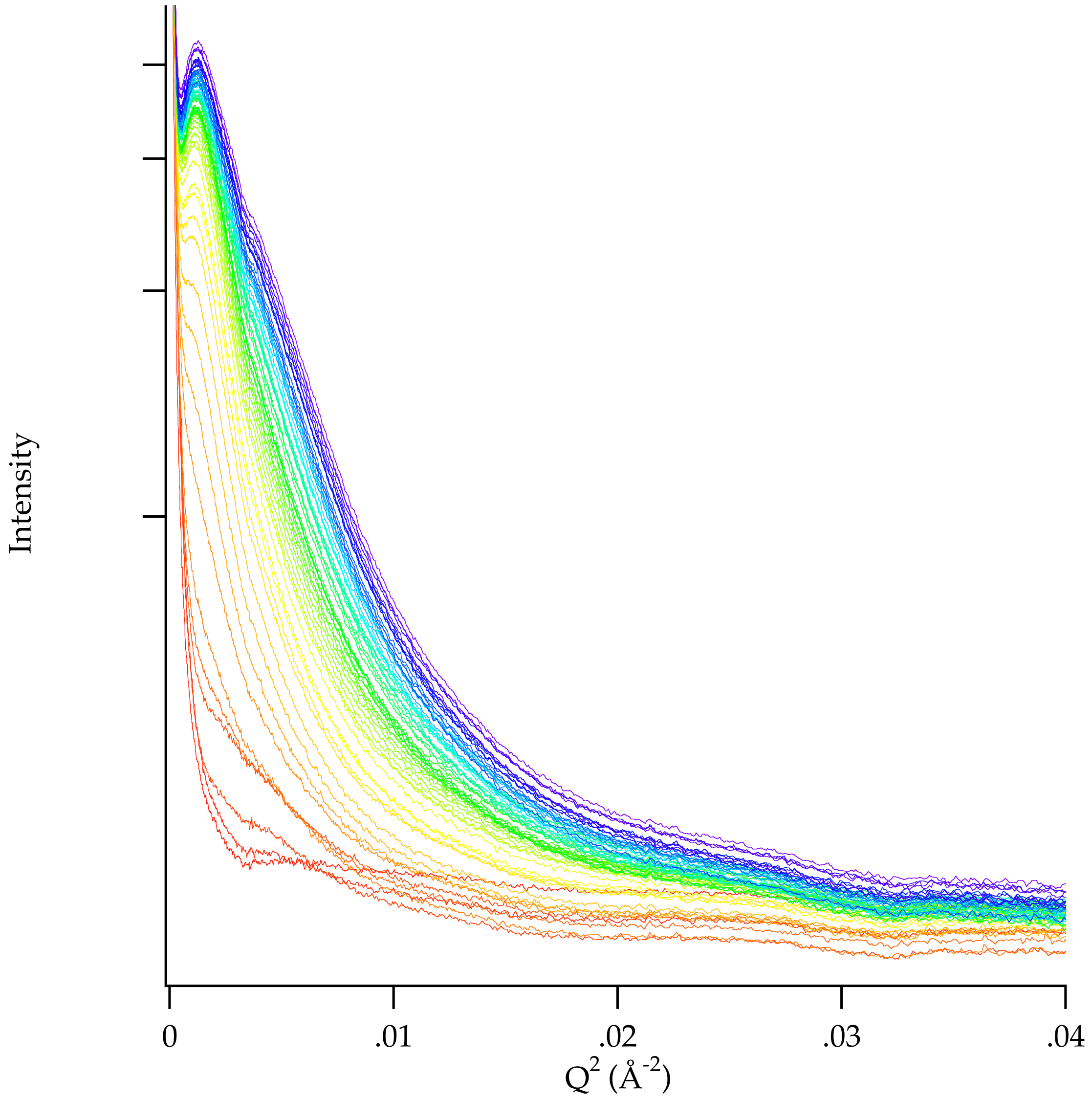

Figure 6.2: in situ SAXS data for Vit101 annealed at 769 K

Logarithm of the scattered intensity vs. Q^2.

The scattered intensity exhibits an interference maximum with a shoulder. The amplitude increases with time.

Differential scanning calorimetry (DSC)

Vit101 samples that were annealed at temperatures similar to those in the small angle X-ray scattering experiments were subsequently studied by DSC [47]. Figure 6.3 shows DSC traces of an as-prepared sample and several annealed samples. There are three distinct exothermic events in the DSC trace of the as-prepared sample. In the annealed samples one or more of the peaks have become smaller or disappeared entirely, indicating that the crystallization events corresponding to those peaks have already occurred during the annealing.

6.2. Discussion

Small angle scattering yields information about the size and spacing of the scattering structures. According to the Guinier approximation for small angle scattering from a particle, the slope in a plot of the logarithm of the scattered intensity vs. Q squared is proportional to the size of the particle. A correlated arrangement of scattering particles will result in an interference maximum in the scattered intensity. The inverse of the Q value where this maximum occurs is a typical spacing of the particles.

The SAXS data was analyzed using the following ad hoc expression for the radial average scattered intensity as a function of Q:

$$C_1 + C_2 Q^n + \frac{C_3}{1 + \exp\left(\frac{\mu^2 - Q^2}{\sigma}\right)} \exp\left(-\frac{R_g^2 Q^2}{3}\right), \tag{6.1}$$

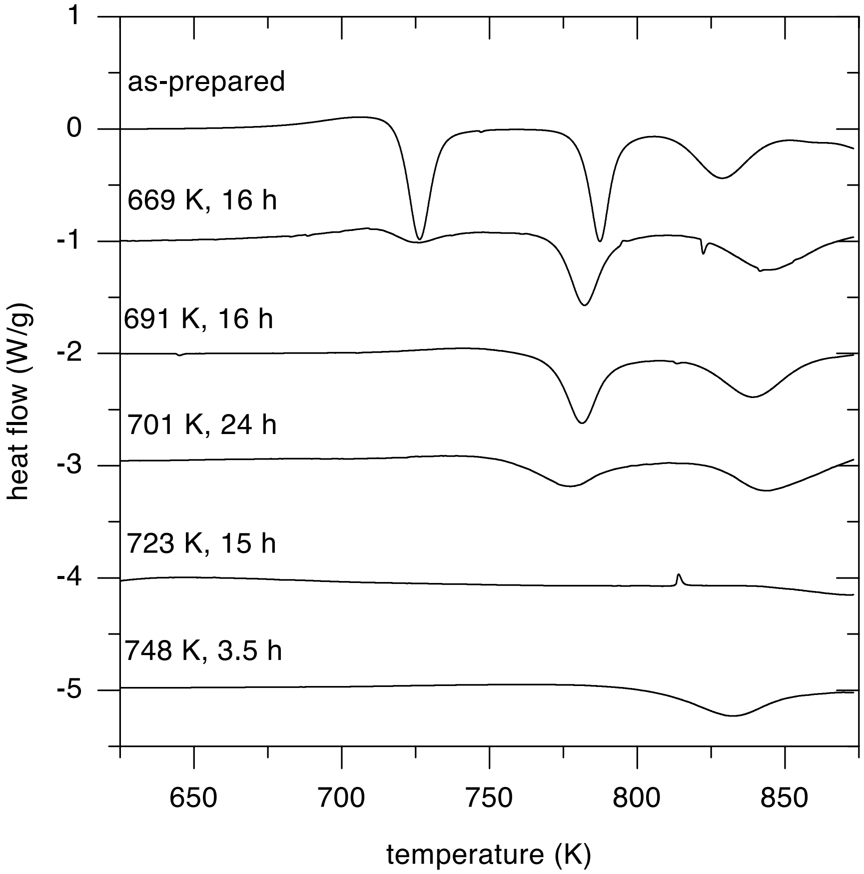

Figure 6.3: DSC traces of annealed Vit101 samples

The direction for exothermic events is down. Traces are offset by multiples of 1 W/g to separate them from eachother.

where the parameters C_1, C_2, n, C_3, R_g, μ, σ, and their evolution with annealing time, were obtained from non-linear least squares regressions. The first term accounts for a constant shift in the baseline, the second term accounts for surface scattering (ideally with an exponent of -2), and the third term embodies the Guinier approximation for scattering from the crystals, multiplied by an envelope function to account for interference. C_1, C_2, C_3 are the intensities for the three terms, n is the adjustable exponent in the surface scattering term, μ is (approximately) the position of the interference maximum, σ is a shape factor for the envelope function $\left(1 + \exp\left(\frac{\mu^2 - Q^2}{\sigma}\right)\right)^{-1}$, and R_g is the Guinier radius of gyration.

The evolution of the radius of gyration R_g thus obtained for samples annealed at different temperatures is plotted in Fig. 6.4. It increases initially, but surprisingly decreases again in the later stages. At higher annealing temperatures this decrease is more pronounced and occurs after shorter annealing times. It was noted that in Fig. 6.2 a shoulder develops precisely where the slope should be measured to evaluate the Guinier radius. It is concluded that the decrease in R_g is related to the development of this shoulder rather than a decrease in the size of the crystals that grew earlier.

When the temperatures of the SAXS experiments are compared with the DSC trace of the as-prepared sample, the interpretation of the shoulder in the SAXS data and of the decrease in R_g becomes clear. The first exothermic event in the DSC trace would have occurred in each of the SAXS experiments. In the SAXS experiments at 754 K and at 769 K, the second exothermic event in the DSC trace would have passed as well. The DSC trace for the sample annealed at 669 K reveals that even at this lower temperature the second event would probably have begun on the time scale of the SAXS experiments.

Thus, during each of the SAXS experiments two separate crystallization processes contributed to the evolution of the scattered intensity. The superposition of these

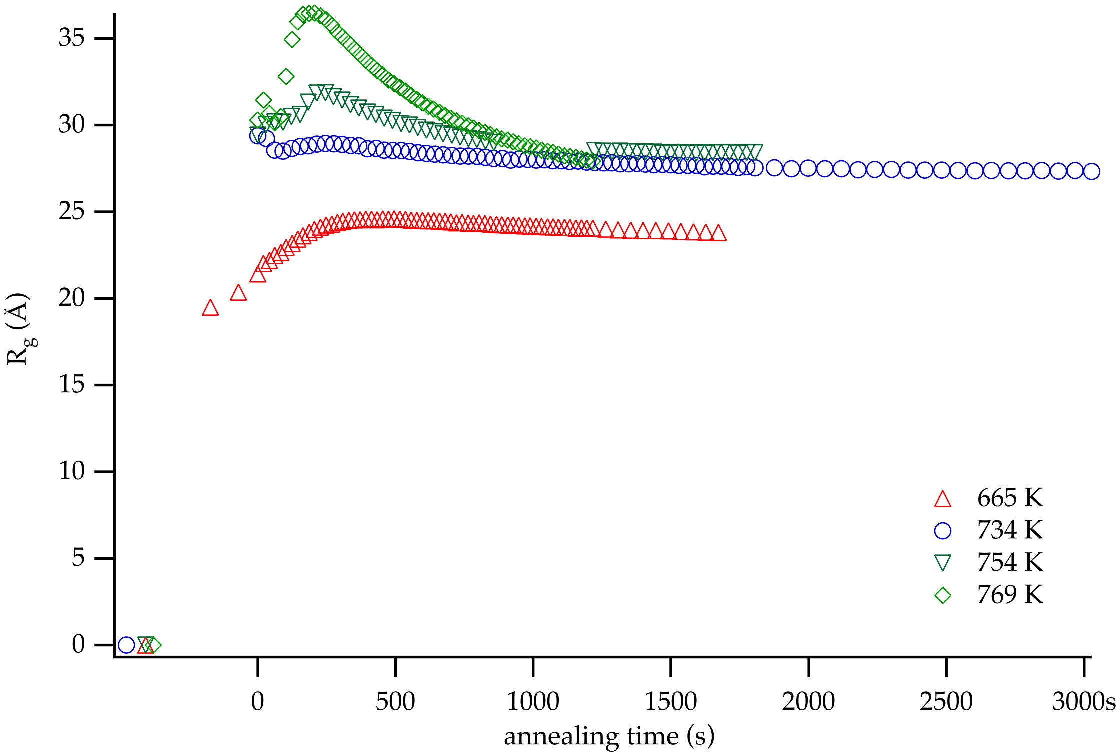

Figure 6.4: evolution of Guinier radius from SAXS

two contributions leads to the shoulder observed in Fig. 6.2. Even though a shoulder is not seen in Fig. 6.1, a decrease is observed in the R_g measured on the corresponding data set for annealing times longer than 500 s. It is concluded that the second crystallization event contributes to the SAXS intensity in each of the experiments.

7. Summary

The solidification microstructure in wedge-shaped castings was investigated, for a series of alloys with compositions systematically varied around $Cu_{47}Ni_8Ti_{34}Zr_{11}$. Near the critical thickness for glass formation, a spatially inhomogeneous dispersion of nanocrystals was observed, where spherical regions contain a much higher density of nanocrystals than the surrounding material. This microstructure is inconsistent with the prevalent theories for crystallization in metallic glasses, which predict a spatially uniform distribution of crystals.

The spatial localization of the nucleation density was attributed to a recalescence instability. When the heat of crystallization was included in the Fourier heat flow equation, coupling the crystal nucleation and growth rates to the heat flow problem, stable solutions were found only under certain conditions. In deeply undercooled liquids, where the nucleation rate increases with temperature, these conditions are never met, and recalescence can occur locally, triggered by a small fluctuation in the early stages of the crystallization process. It was argued that because the localized recalescence events and their interaction accelerate crystallization, they are important in determining the glass forming ability as well as the microstructure of these alloys.

The composition dependence of the critical thickness for glass formation, determined from the observed microstructures, and in situ small angle scattering results acted as a reminder that crystallization in glass forming alloys is a complex process involving several competing crystalline phases.

A. Appendices

A.1. Properties of Vit101

Table A.1: physical properties of Vit101

Name	Symbol	Value	Units
average atomic mass	MW	60.884	g/mol
density	ρ	6.85×10^{3}	kg/m^3
molar volume	V_{mol}	8.89×10^{-6}	m^3/mol
average atomic volume	V_{at}	1.48×10^{-29}	m^3
average atomic radius	r_{at}	1.52×10^{-10}	m
liquidus temperature	T_{liq}	1128	K
heat of fusion	ΔH_{f}	11.3×10^{3}	J/mol
interfacial tension	σ_{sl}	100 – 150	J/m^2
glass transition temperature	T_{g}	671	K
heat capacity	c_{P}	45	$J/(mol\cdot K)$
thermal conductivity	κ	25	$W/(m^2K)$
thermal diffusivity	α	5×10^{-6}	m^2/s
Vogel-Fulcher temperature	T_{VF}	500	K
fragility index	D	12	-
Vogel-Fulcher prefactor	η_{∞}	4.49×10^{-5}	$Pa\cdot s$

A.2. Solutions to the Fourier heat flow equation

Application of spectral theory

The Laplacian appearing in the Fourier heat flow equation (Eq. 2.1) is a linear operator on the Hilbert space of all functions which satisfy the boundary conditions. The Laplacian therefore has a spectral representation [48], which can be used to solve the Fourier heat flow equation. With rectangular boundary conditions, the spectral representation of the Laplacian is the familiar Fourier transform*. The spectral representation of the Laplacian transforms the heat flow equation, a partial differential equation in $T(x, t)$, into an infinite set of first-order ordinary differential equations in the spectral coefficients $\theta_k(t)$:

$$\frac{\partial\theta_k}{\partial t} = -\alpha k^2 \theta_k(t) \tag{A.1}$$

where $-k^2$ is the improper eigenvalue of the Laplacian corresponding to the improper eigenfunction $T_k(x)$, i.e., $\nabla^2 T_k(x) = -k^2 T_k(x)$. The solution to the Fourier heat flow equation projected on these eigenfunctions is:

$$T(x, t) = \sum_k \theta_k(t) T_k(x) \tag{A.2}$$

The solutions of Eq. A.1 for the coefficients $\theta_k(t)$ are exponentials decaying with a time constant $\tau = 1/(\alpha k^2)$:

$$\theta_k(t) = \theta_k(0) e^{-\alpha k^2 t} \tag{A.3}$$

---

* Spectral theory provides the generalization of the Fourier transform method for solving the heat flow equation with boundary conditions other than rectangular or infinite.

Thus, a general solution to the Fourier heat flow equation is given by

$$T(x, t) = \sum_k \theta_k(0) e^{-\alpha k^2 t} T_k(x) \tag{A.4}$$

where the boundary conditions are represented by the form of the eigenfunctions $T_k(x)$ and the initial conditions determine the initial values $\theta_k(0)$ of the spectral coefficients.

E.g., in one dimension, spectral representation is a Fourier series:

$$T(x, t) = \sum_k \theta_k(t) \sin(kx) \quad \text{with } \theta_k(t) = \frac{1}{2L}\int_0^L T(x, t) \sin(kx) dx \tag{A.5}$$

and the solution to the heat flow equation can be written as

$$T(x, t) = \frac{1}{2L}\sum_k e^{-\alpha k^2 t} \left\{ \int_0^L T(x)\big|_{t=0} \sin(kx) dx \right\} \sin(kx) . \tag{A.6}$$

Unfortunately, Fourier expansions do not converge very well near discontinuities, a fact which limits the usefulness of this expression in describing the early stages of heat flow. In the late stages, the short wavelength terms have all decayed away, and the fundamental harmonic dominates, decaying with a time constant $\tau = L^2/(\pi^2 \alpha)$.

Heat flow in a flat plate

For a plate of constant thickness where the width and height are much greater than the thickness, cooled from the surface, the temperature profile is to a good approximation one-dimensional. The initial condition is $T(x)|_{t=0} = T_\infty$ and the boundary conditions are $T(t)|_{x=0} = T(t)|_{x=L} = T_0$. Eq. A.6 then results in

$$T(x, t) = T_0 + (T_\infty - T_0) \sum_{k = \frac{(2n+1)\pi}{L}} \frac{1}{kL} e^{-\alpha k^2 t} \sin(kx). \qquad \text{(A.7)}$$

Fig. A.1 shows the evolution over time of this temperature profile with typical values for the physical parameters.

Heat flow at a semi-infinite wall

In the early stages of any heat flow problem where the initial temperature is uniform, the temperature remains uniform except near the surface. If the surface is planar or if its radius of curvature is sufficiently large, the heat flow near the surface can be treated as a limit of the previous case where $L \to \infty$. The summation in Eq. A.7 is then replaced by an integral:

$$T(x, t) = T_0 + (T_\infty - T_0) \int_0^\infty \frac{1}{k} e^{-\alpha k^2 t} \sin(kx) dk, \qquad \text{(A.8)}$$

which in this case can be solved analytically:

$$\int_0^\infty \frac{1}{k} e^{-\alpha k^2 t} \sin(kx) dk = \int \left\{ \int_0^\infty e^{-\alpha k^2 t} \sin(kx) dk \right\} dx = \int e^{-\frac{x^2}{4\alpha t}} dx = \mathrm{erf}\left(\frac{x}{\sqrt{4\alpha t}}\right), \qquad \text{(A.9)}$$

resulting in the final answer:

$$T(x, t) = T_0 + (T_\infty - T_0) \mathrm{erf}\left(\frac{x}{\sqrt{4\alpha t}}\right). \qquad \text{(A.10)}$$

This temperature profile, with the same parameters as in Fig. A.1, is displayed in Fig. A.2.

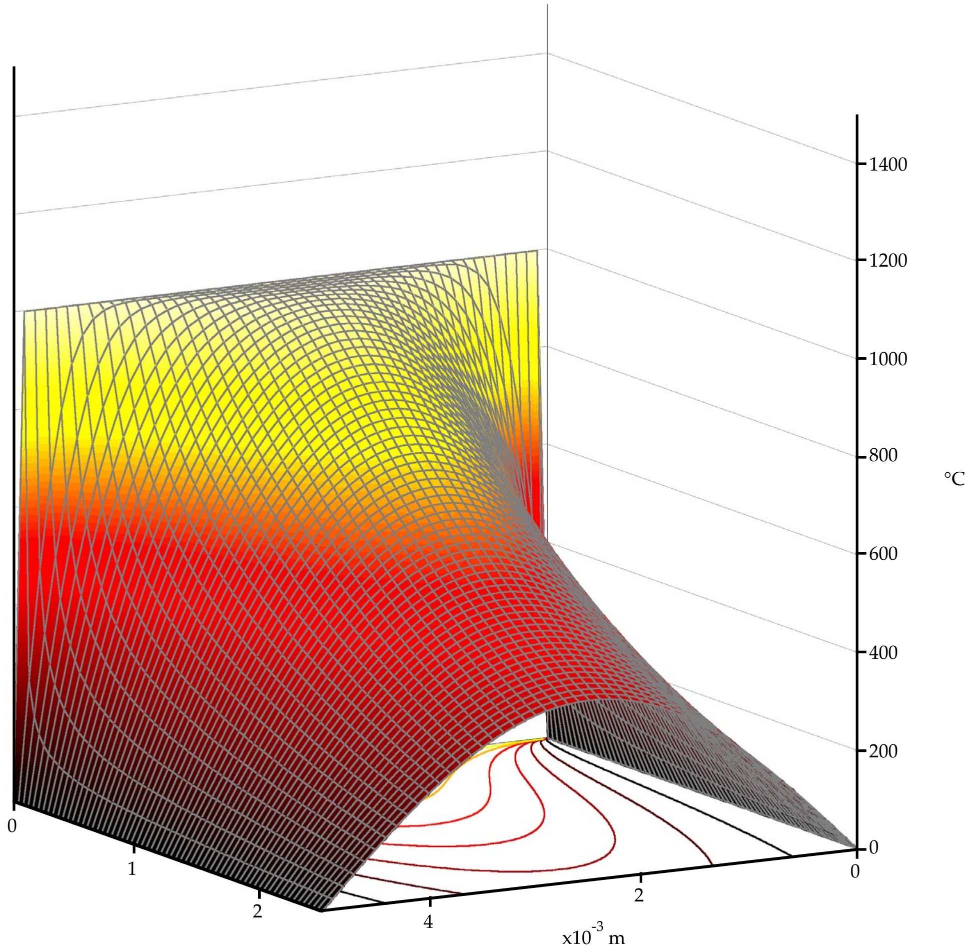

Figure A.1: temperature profile evolution in a flat plate

thermal diffusivity: $1.25\times10^{-6} m^2/s$

thickness: 5 mm

initial temperature: 1000 °C

mold temperature: 0 °C

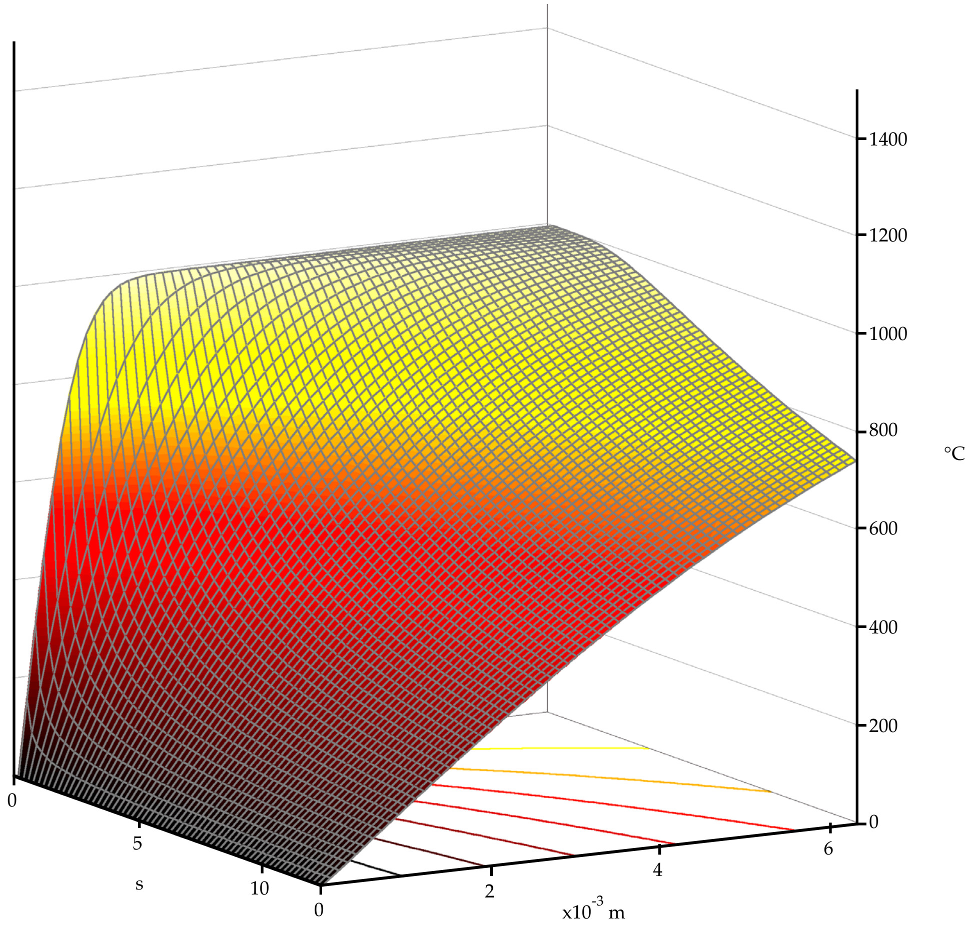

Figure A.2: temperature profile evolution at semi-infinite wall

thermal diffusivity: $1.25 \times 10^{-6} m^2/s$

initial temperature: 1000 °C

mold temperature: 0 °C

A.3. Geometry of composition spaces

The composition of an n-component alloy is completely specified by the amounts of each of the n components present in the alloy. However, the total amount of the alloy does not influence the composition, so there are $n - 1$ compositional degrees of freedom. Mathematically this is expressed as a normalization: the n-dimensional vector space of the amount of each of the components is projected onto the $n - 1$ dimensional surface where the norm is equal to 1.

The choice of the normalization function is somewhat arbitrary. It corresponds to the choice of units for the amounts of the different components, although in principle other normalization functions (without physical meaning) could also be considered. A different norm function will define a projection onto a different composition space. For example, compositions are commonly expressed as either mole fractions or mass fractions, and some stretching is necessary to convert a graphical representation of one to the other. In this case, both normalization functions are linear, so the transformation from one to the other is linear in the original n-dimensional space. As a result, a straight line remains a straight line in the $n - 1$ dimensional space, even though angles and relative distances change. This is not true if —in the chosen units, volume for example— the total amount is not conserved on mixing, which corresponds to a non-linear normalization function.

The constraint that the amounts of each of the components must be positive translates into a set of n symmetric linear bounds on the $n - 1$ dimensional composition space. The physically meaningful compositions are therefore constrained to the $n-1$ dimensional generalization of a tetrahedron. As shown in Fig. A.3, the physically meaningful compositions are therefore constrained to the linear interval [0,1] for a 2-component system, to an equilateral triangle for a 3-component system, to a regular tetrahedron for a 4-component system, etc… The full dimensionality of the composition space of a system with 4 or more components is hard to visualize in 2 dimensions. Such composition spaces are usually represented by a projection onto a pseudo-ternary diagram, either by ignoring some of the components or grouping several together at one of the vertices of the triangle.

The highly symmetrical nature of composition spaces (and the difficulty of visualizing the full dimensionality of the composition space of a system with more than 4 components) illustrate that although the composition space has only $n-1$ degrees of freedom, it is often more convenient to think of it as the projection of an n-dimensional space.

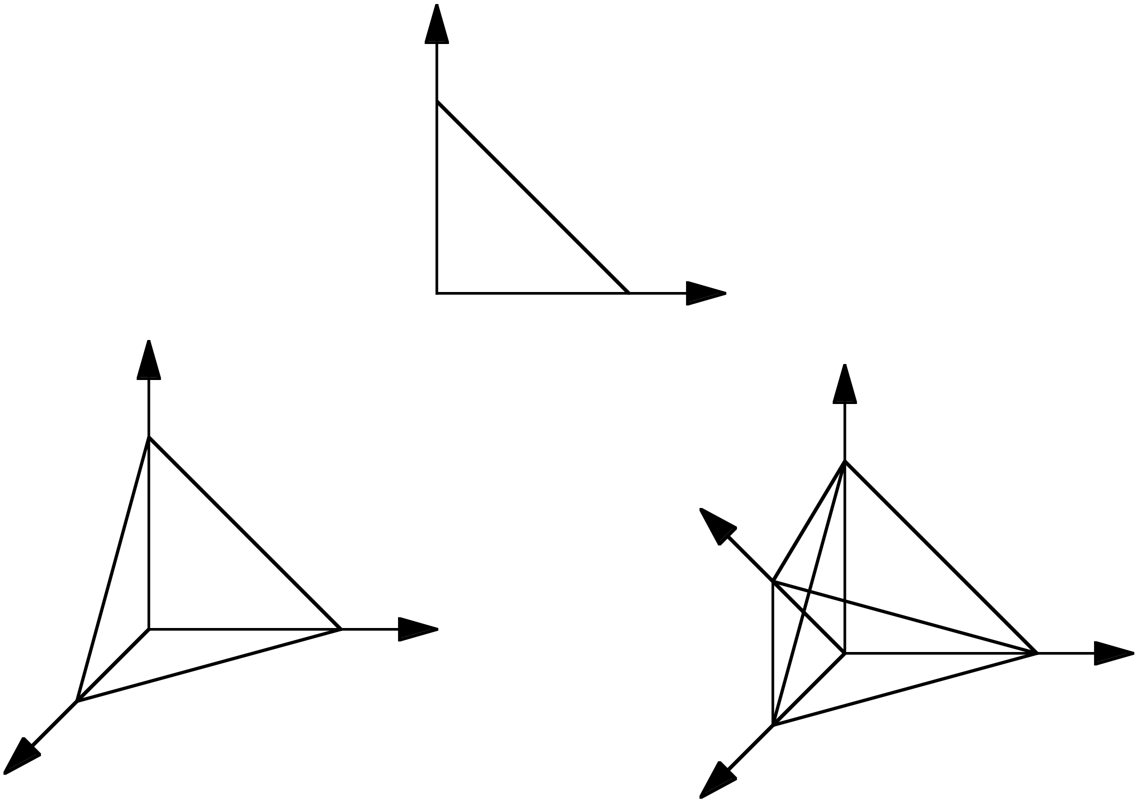

Figure A.3: geometry of composition spaces

> *Normalized composition spaces for n-component system: a linear interval for 2 components, an equilateral triangle for 3 components, a regular tetrahedron for 4 components and the* $n-1$ *dimensional generalization of a tetrahedron in general.*

References

1. C. A. Angell, Science **267**, 1924 (1995).
2. *Binary Alloy Phase Diagrams*; Eds. T. B. Massalski, H. Okamoto, P. R. Subramanian, L. Kacprzak (William W. Scott, Jr., ASM International, 1990).
3. Yunus A Çengel, *Heat Transfer: A Practical Approach* (McGraw-Hill, 1998).
4. F. Press and R. Siever, *Understanding Earth* (Freeman, 1997), p. 78.
5. R. Cotterill, *The Cambridge Guide to the Material World* (Cambridge University Press, 1985), Chap. 11.
6. H.-G. Elias, *An Introduction to Plastics* (VCH, 1993), Chap. 4.
7. W. Klement, R. Willens, and P. Duwez, Nature **187**, 869 (1960).
8. H. L. Luo and P. Duwez, Appl. Phys. Lett. **2**, 21 (1963).
9. P. Duwez, R. Willens, and R. C. Crewdson, J. Appl. Phys. **36**, 2267 (1965).
10. P. Duwez and S. C. H. Lin, J. Appl. Phys. **38**, 4096 (1967).
11. N. DeCristofaro, MRS Bulletin **23**, 50 (1998).
12. A. Inoue, T. Zhang, and T. Masumoto, Mater. Trans. JIM **31**, 425 (1990).
13. T. Zhang, A. Inoue, and T. Masumoto, Mater. Trans. JIM **32**, 1005 (1991).
14. A. Peker and W. L. Johnson, Appl. Phys. Lett. **63**, 2342 (1993).
15. A. Inoue, N. Nishiyama, and H. Kimura, Mater. Trans. JIM **38**, 179 (1997).
16. C. C. Hays, J. Schroers, U. Geyer, S. Bossuyt, N. Stein, and W. L. Johnson, Materials Science Forum **343-3**, 103 (2000).
17. X. H. Lin and W. L. Johnson, J. Appl. Phys. **78**, 6514 (1995).
18. J. T. Armstrong, Microbeam Analysis **4**, 177 (1995).
19. J. Schroers, unpublished research.

20. C. C. Hays, unpublished research.

21. B. E. Warren, *X-ray Diffraction* (Addison-Wesley, 1969; Dover, 1990), Chap. 10.

22. B. E. Warren, *X-ray Diffraction* (Addison-Wesley, 1969; Dover, 1990), Chap. 13.

23. D. Turnbull and M. H. Cohen, J. Chem. Phys. **29**, 1049 (1958).

24. D. Turnbull, Contemp. Phys. **10**, 473 (1969).

25. J. W. Christian, *The Theory of Transformations in Metals and Alloys* (Pergamon), Chap. 10.

26. K. F. Kelton, Solid State Phys. **45**, 75 (1991).

27. A. Masuhr, Ph. D. Thesis, California Institute of Technology, 1999.

28. D. A. Porter and K. E. Easterling, *Phase Transformations in Metals and Alloys* (Chapman & Hall, 1992), Chap. 4.

29. Y. J. Kim, R. Busch, W. L. Johnson, A. J. Rulison, and W. K. Rhim, Appl. Phys. Lett. **68**, 1057 (1996).

30. D. R. Askeland, *The Science and Engineering of Materials* (Chapman & Hall, 1990).

31. J. C. Foley, D. R. Allen, and J. H. Perepezko, Scr. Mater. **35**, 655 (1996).

32. R. Busch, S. Schneider, A. Peker, and W. L. Johnson, Appl. Phys. Lett. **67**, 1544 (1995).

33. S. Schneider, P. Thiyagarajan, and W. L. Johnson, Appl. Phys. Lett. **68**, 493 (1996).

34. J. F. Löffler and W. L. Johnson, Appl. Phys. Lett. **76**, 3394 (2000).

35. K. F. Kelton, Philos. Mag. Lett. **77**, 337 (1998).

36. S. C. Glade, R. Busch, D. S. Lee, W. L. Johnson, R. K. Wunderlich, and H. J. Fecht, J. Appl. Phys. **87**, 7242 (2000).

37. R. K. Wunderlich, D. S. Lee, W. L. Johnson, and H. J. Fecht, Phys. Rev. B **55**, 26 (1997).

38. H. A. Davies, Phys. Chem. Glasses **17**, 159 (1976).

39. F. Spaepen and D. Turnbull, Rapidly Quenched Met. **2**, 205 (1976).

40. D. Holland-Moritz, J. Schroers, D. M. Herlach, B. Grushko, and K. Urban, Acta Mater. **46**, 1601 (1998).

41. H. W. Kui, A. L. Greer, and D. Turnbull, Appl. Phys. Lett. **45**, 615 (1984).

42. X. H. Lin, W. L. Johnson, and W. K. Rhim, Mater. Trans. JIM **38**, 473 (1997).

43. C. Angell, J. Phys. Chem. **100**, 13211 (1996).

44. R. B. Ash, *Information Theory* (Wiley, 1965; Dover, 1999), Chap. 8.

45. X. H. Lin, Ph. D. Thesis, California Institute of Technology, 1996.

46. J. C. Foley, D. J. Sordelet, and T. A. Lograsso, in *Mat. Res. Soc. Proc.* **554**, 199 (Materials Research Society, 1999), Eds. W. L. Johnson, A. Inoue and C. T. Liu; D. J. Sordelet, private communication.

47. S. C. Glade, J. F. Löffler, S. Bossuyt, W. L. Johnson, and M. K. Miller, to be published in J. Appl. Phys.

48. B. Friedman, *Principles and Techniques of Applied Mathematics* (Wiley, 1956; Dover, 1990).